Draft version December 10, 2014
Preprint typeset using LaTeX style emulateapj v. 5/2/11

VARIATIONS OF THE ISM CONDITIONS ACROSS THE MAIN SEQUENCE OF STAR FORMING GALAXIES: OBSERVATIONS AND SIMULATIONS

J. R. Martínez-Galarza[1], H. A. Smith[1], L. Lanz [2], Christopher C. Hayward[3,1], A. Zezas[4,1], L. Rosenthal[5], A. Weiner[1,6], C. Hung[1,7], M. L. N. Ashby[1], B. Groves[8]

Draft version December 10, 2014

ABSTRACT

Significant evidence has been gathered suggesting the existence of a main sequence (MS) of star formation in galaxies. This MS is expressed in terms of a correlation between the star formation rate and the stellar mass of the form SFR $\propto M_*^{\alpha}$ and spans a few orders of magnitude in both quantities. Several ideas have been suggested to explain fundamental properties of the MS, such as its slope, its dispersion, and its evolution with redshift. However, no consensus has been reached regarding its true nature, or whether the membership of particular galaxies to this MS implies the existence of two different modes of star formation. In order to advance our understanding of the MS, here we use a statistically robust Bayesian Spectral Energy Distribution (SED) analysis (Chiburst) to consistently analyze the star-forming properties of a set of hydro-dynamical simulations of mergers, as well as observations of real mergers and luminous galaxies, both local and at intermediate redshift. We find a very tight correlation between the specific star formation rate (sSFR) of our fitted galaxies, and the typical conditions of the star-forming interstellar medium (ISM), parametrized via a novel quantity: the compactness parameter $\mathcal{C}$, that controls the evolution of dust temperature with time. The normalization of this correlation is bimodal, and such bi-modality relates to the membership of individual galaxies to the MS. As mergers move into the coalescence phase, they increase their compactness and sSFR, creating a scatter in the MS that we measure to be 0.38 dex. The increase in compactness implies that the physical conditions of the ISM smoothly evolve across the MS. One possible interpretation for the slope of the $\log$ sSFR-$\log \mathcal{C}$ correlation is that systems with higher sSFR have smaller physical sizes, whereas the bi-modality between MS objects and outliers suggests the existence of two different regimes of star formation, with distinct ISM conditions.

1. INTRODUCTION

Over the last decade, deep optical and infrared surveys have established that the majority of star-forming galaxies up to $z = 2.5$ follow a simple scaling correlation linking their stellar mass with their star formation rate (SFR): SFR $= M_*^{\alpha}$, with $0.5 < \alpha < 1.0$ (Brinchmann et al. 2004; Noeske et al. 2007; Elbaz et al. 2007; Daddi et al. 2007). The bulk of star-forming galaxies that lie near this simple correlation have been collectively called the "main sequence" (MS) of star-forming galaxies. The existence of a MS has been interpreted as evidence that the majority of galaxies throughout cosmic history form stars in a steady, secular mode, in time scales that are longer than their dynamical timescales (Genzel et al. 2010; Wuyts et al. 2011), a mode that requires a continuous replenishment of gas from the intergalactic medium. In this picture, the outliers above the MS would be explained by starburst events, probably triggered by mergers, with shorter depletion timescales yielding larger sSFRs for systems off the MS. It has been noted that the zero-point of the MS evolves with redshift, with the MS in the intermediate- and high-z Universe located higher in SFR with respect to the local MS. A possible interpretation of this behavior is given in terms of a larger $f_{\rm gas}$ in galaxies earlier in cosmic history (e.g., Combes 2012, and references therein).

Both simulations (e.g., Davé et al. 2011; Torrey et al. 2014; Sparre et al. 2014) and semi-analytical models (e.g. Dutton et al. 2010; Davé et al. 2012; Dekel et al. 2013; Mitchell et al. 2014) predict the existence of the MS and qualitatively reproduce the redshift dependence of the normalization. In these models, the redshift evolution is driven by evolution in the gas accretion rates onto galaxies. The scatter in the MS at fixed stellar mass, which is 0.2-0.4 dex, may be caused by variations in gas accretion rates, formation histories, environment, or galaxy structure, among other possible causes. Merger-induced starbursts can cause galaxies to temporarily move significantly above the MS, but state-of-the-art cosmological hydrodynamical simulations underpredict the abundance of MS outliers (Sparre et al. 2014). This underprediction may suggest that other processes, such as violent disk instability (e.g. Ceverino et al. 2010; Porter et al. 2014) may be an important source of outliers above the MS.

Interestingly, the existence and redshift evolution of the MS may simply be a consequence of the central limit theorem if in situ star formation is a (perhaps correlated) stochastic process (Kelson 2014). Thus, the ap-

[1] Harvard-Smithsonian Center for Astrophysics, 60 Garden Street, Cambridge, MA 02138, USA, jmartine@cfa.harvard.edu
[2] Infrared Processing and Archival Center, California Institute of Technology, MC 100-22, Pasadena, CA 91125, USA
[3] TAPIR 350-17, California Institute of Technology, 1200 E. California Blvd., Pasadena, CA 91125, USA
[4] University of Crete, Physics Department, P.O. Box 2208, 710 03 Heraklion, Crete, Greece
[5] Haverford College, 370 Lancaster Ave, Haverford, PA 19041, USA
[6] RPI Institute, 110 8th St, Troy, NY 12180, USA
[7] Institute for Astronomy, 2680 Woodlawn Drive, Honolulu, HI 96822-1839, USA
[8] Max-Planck-Institut fr Astronomie, Knigstuhl 17, 69117, Heidelberg, Germany

proximately linear slope and the redshift evolution of the MS may not be a useful constraint on theoretical models. However, the magnitude of the scatter in the MS and the populations of outliers, both significantly above (i.e. starbursts) and below (i.e. quenched galaxies) the MS may be able to provide more useful physical constraints on models. Thus, it is of utmost importance to constrain possible variations in physical properties of galaxies across the MS.

The idea of galactic collisions as one possible driving force behind the most spectacular episodes of star formation in the local Universe is supported by the fact that ultra-luminous infrared galaxies (ULIRGs) are often undergoing major merger events, with compact nuclear starbursts providing most of the infrared luminosity (Veilleux et al. 2002). It seems therefore natural to associate outliers of the MS with such starburst events, although it has been noted that mergers are not necessary to explain the existence of ULIRGs in the high-z Universe (e.g., Sturm et al. 2010), or in other words, that the incidence of mergers in ULIRGs declines with redshift.

Regarding this difference between local and high redshift ULIRGs, Elbaz et al. (2011) argue, based on the analysis of a deep ($z < 2.5$) survey in the Great Observatories Origins Deep Survey (GOODS)-*Herschel* program, that whereas local ULIRGs belong to the starburst mode of star formation, their high-z counterparts are forming stars in the MS domain, and that the resulting confusion between these two flavors of ULIRGs would explain the "mid-IR excess" population observed in $z > 1.5$ galaxies (Daddi et al. 2007; Papovich et al. 2007). In the same paper they propose the existence of an infrared MS defined in terms of the ratio of total infrared luminosity to 8 μm luminosity, which has a Gaussian distribution centered at $L_{\rm IR}/L_{8\mu{\rm m}} = 4$ ($\sigma = 1.6$). They associate the outliers of this infrared MS with a starburst mode of star formation, and find that these outliers are systems with compact projected star formation densities. In this scenario, it is unclear whether the transition from the MS to the outlier regime is a gradual process, or if it happens abruptly.

Despite impressive recent observational and theoretical progress, the MS paradigm and its interpretation in terms of secular vs. starbursty star-formation faces at least two major challenges. The first of these challenges has to do with the suitability of far-infrared (FIR) studies in probing the MS, since they are biased towards systems with high SFR. For instance, Lee et al. (2013) combine multi-wavelength photometry of a sample of over 4000 *Herschel*-selected galaxies in the Cosmic Evolution Survey (COSMOS) field in the redshift range $z = 0.02 - 3.54$ and find that $\sim 60\%$ of these galaxies are more than 1σ above the adopted values for the MS at several redshifts. They also find no evidence for a constant $L_{\rm IR}/L_{8\mu{\rm m}}$ value in high redshift ULIRGs, a feature that had been reported in Elbaz et al. (2011) and dubbed as the infrared MS of star-forming galaxies. The second challenge has to do with the interpretation of the scatter across the MS, and whether the membership or not of particular galaxies to the MS underlies the existence of two different modes of star formation (i.e., different physical conditions of the gas and dust on and off the MS). Whereas some authors (Hayward et al. 2012; Magnelli et al. 2014) have recently argued that the evolution of $T_{\rm dust}$ with sSFR implies a difference in the physical conditions of the interstellar medium (ISM) in starbursts as compared to MS galaxies, other studies have suggested that the distance from a particular galaxy to the locus of the MS depends only on the ratio of gas mass to stellar mass $f_{\rm gas} = M_{\rm gas}/M_*$ (Magdis et al. 2012), with invariance of the ISM physics.

It is therefore important to tackle this problem with as many tools as we have at hand, to try to solve these fundamental questions. It is well established that the bulk of galaxies that constitute the MS are non-interacting systems, but the role of interactions in shaping the properties of the MS is not well understood. Hydrodynamical simulations of isolated and interacting systems whose properties that we can use in combination with the observations come in extremely handy for this task. In this paper, we use a statistically robust SED analysis method (CHIBURST) based on the star-forming galaxy models of Groves et al. (2008), to consistently analyze the star-forming properties of a set of hydro-dynamical simulations of mergers and compare them with real observations of local mergers, local luminous ($L > 10^{11}$ L$_\odot$) mergers, and intermediate redshift ULIRGs, with the goal of characterizing the MS, and providing physically-based explanations to the main properties of the MS (its slope, scatter, and evolution with redshift).

Our methodology is simple: we first apply CHIBURST to the multi-wavelength mock SEDs of a set of simulated mergers. The SEDs were calculated by performing dust radiative transfer in post-processing on hydrodynamical simulations. For calibration purposes, we compare the *a priori* known global properties of the simulated systems, such as stellar mass, SFR, and dynamical time, to the SED-derived typical ISM conditions of their internal star-forming regions. We then apply the same method to a selection of 24 local interacting galaxies at different stages, 6 local luminous ($L > 10^{11}$ L$_\odot$), late-type mergers, and 9 $z \sim 0.3$ ULIRGs for which ultraviolet to FIR photometry was available. Starting from the derived properties, we search for correlations between global and local physical properties and discuss our results in terms of the MS of star formation and the implications for its general properties. Finally, we discuss possible variations of the internal physical conditions in galaxies as they move along and across the MS.

The paper is structured as follows. In §2 we describe the observations of interacting galaxies used in this paper as well as the reduction process used to obtain their SEDs. In §3 we give an overview of the hydrodynamical models and the radiative transfer code used to generate the mock SEDs of interacting systems. We present CHIBURST, our novel Bayesian Monte Carlo fitting method in §4, and in §5 we show the results of applying it to both the observed galaxies and the simulated ones. We discuss the correlations found and their implications for massive star formation in §6. Finally, we summarize our findings in §7.

2. OBSERVATIONS

The sample of observed galaxies analyzed here comprises three different groups: *(i):* a subsample of 27 local interactions from the Spitzer Interactive Galaxy Survey (SIGS); *(ii):* an additional group of 6 local, luminous ($> 10^{11}$ L$_\odot$) stage 4 interactions that we have mor-

phologically selected from the Sloan Digital Sky Survey (SDSS) and Galaxy Zoo and cross checked with the revised IRAC Faint Source Catalog; and *(iii):* a group of 9 *Herschel*-selected intermediate-redshift ($z \sim 3$) ULIRGs from Magdis et al. (2014). We list the observed systems in Table 1.

The SIGS sample is fully described in Brassington et al. (submitted) and was designed to span a broad range of galaxy interaction properties based on their interaction probability, and not only on morphological properties. This was done to guarantee that the sample included systems covering the full range of interaction stages, and not only those with strong morphological disturbances. In this paper we analyze a subsample of 27 interacting galaxies presented in Lanz et al. (2013) (L13 hereafter), which include those SIGS galaxies for which *Herschel* data was available when that paper was prepared. Out of the 31 galaxies in L13, we exclude NGC 3226, NGC 3227 and NGC 3077, because they do not have reliable *GALEX* data. We also exclude NGC 4649, a large elliptical with very little MIR/FIR emission. Additionally, the pairs NGC 3396/3396, NGC 3690/IC694, and NGC 4038/4039 are indistinguishable within a single aperture, which means that we only have their integrated SEDs. We therefor have a total of 24 SEDs if local interactions. In L13, these galaxies have been ranked by interactions stage between stage 1 (isolated, non-interacting galaxies) and stage 4 (strongly interacting galaxies) and all except one (NGC 3690) have luminosities between 0.25×10^9 $L_\odot$ and 9.8×10^10 $L_\odot$. From their MIR colors, none of them appears to be globally dominated by AGN activity.

The photometry for these galaxies is fully described in L13. Briefly, matched apertures were used across all wavebands, choosing in each case the Kron aperture to fully encircle the galaxy in the waveband where it looks more extended. A local background was applied in each case and aperture corrections were applied.

The galaxies in the second group were chosen to extend our sample of local interactions to include bright, late-type interactions that had available *Herschel* observations. They were selected by cross-referencing the *IRAC Faint Source Catalog* with Galaxy Zoo (Lintott et al. 2008) objects that show stage 4 morphology and have luminosities $L > 10^{11}$ $L_\odot$. All six objects selected this way had *Herschel*-PACS and *Hershcel*-SPIRE maps available from the Great Observatories All-sky LIRG Survey (GOALS) (Armus et al. 2009). We obtained the photometry reducing these maps using the Herschel Interactive Processing Environment (HIPE) and performing aperture photometry for our galaxies using the same method as for the L13 galaxies.

Finally, the intermediate-z systems were selected from the original *Herschel* Multi-tiered Extragalactic Survey (Oliver et al. 2012). Only sources with $S_{250} > 150$ mJy in fields covered by the survey, and with available spectrometric redshifts were selected. The redshift range covered is $0.248 < z < 0.366$, except for one object whose redshift is 0.550. The luminosities of these systems are similar to those in the second group of local interactions, although they are all spatially unresolved, and therefore we cannot allege that they are merger systems. The full sample and the photometry extraction is described in Magdis et al. (2014).

3. MOCK PHOTOMETRY OF INTERACTING SYSTEMS

To provide us with a control sample of simulated mergers, we use the same set of hydrodynamical simulations described in Lanz et al. (2014) (L14 hereafter). Here we will briefly describe those aspects of the simulations that are relevant for our discussion. A hydrodynamical code is combined with a radiative transfer code to obtain mock SEDs at different times for a combination of 4 isolated progenitor galaxies and the 10 possible mergers arising from interactions between every different pair of progenitors. The hydrodynamical calculations are performed using the GADGET-3 code (Springel 2005), while the radiative transfer is calculated using the 3D Monte Carlo dust radiative transfer code SUNRISE (Jonsson 2006; Jonsson et al. 2010). The methods for combining the output from the hydrodynamical code with the dust physics for particular types of galaxies are described in Narayanan et al. (2010a,b); Hayward et al. (2011) and Hayward et al. (2012). The progenitor galaxies are similar to typical Sloan Digital Sky Survey (SDSS) galaxies, with masses ranging from 6×10^8 $M_\odot$ to 4×10^{10} $M_\odot$. In addition to the mergers described in L14, here we also include a more massive, gas-rich merger intended to represent a typical submillimeter galaxy (SMG). We list the basic properties for our simulated mergers in Table 2.

The emerging SEDs of these systems are computed for ~ 100 snapshots spanning a time range of ~ 6 Gyr. The time between snapshots is 100 Myr, although a finer time resolution (10 or 20 Myr) is used near the peaks of star formation, for example during the coalescence phase of the interactions. SEDs are obtained for seven different viewing angles. In the case of interacting systems, the galaxy pairs were put in a specific parabolic orbit with initial separations increasing with the mass of the larger galaxy. We obtain mock photometry of the simulated systems by convolving (assuming $z = 0$) the resulting SEDs with the filter response of the following bands: *GALEX*-FUV, *GALEX*-NUV, U, B ,V (Johnson), J, H, K_S (2MASS), *Spitzer*-IRAC 3.6 μm, *Spitzer*-IRAC 4.5 μm, *Spitzer*-IRAC 5.8 μm, *Spitzer*-IRAC 8μm, *IRAS* 12 μm, *Spitzer*-MIPS 24 μm, *IRAS* 25 μm, *IRAS* 60 μm, *Herschel*-PACS 70 μm, IRAS 100 μm, *Herschel*-PACS 100 μm, *Spitzer*-MIPS 160 μm, *Herschel*-PACS 160 μm, *Herschel*-SPIRE 250 μm, *Herschel*-SPIRE 350 μm, and *Herschel*-SPIRE 500 μm.

Unresolved star formation is accounted for by assuming that gas particles with densities above $n \sim 0.1$ cm^{-3} form stars according to the volume-density-dependent Schimdt-Kennicut law $\dot{\rho_*} \propto n_{\rm gas}^{\alpha}$, with $\alpha = 1.5$ (Schmidt 1959; Kennicutt 1998). Due to the limited mass resolution of the simulations, individual stars are not created. Instead, equal mass star particles are generated stochastically such that the SFR obtained in this way agrees with the Kennicutt law. For all snapshots in each simulation, we register the following quantities: the instantaneous SFR ($\rm SFR_{inst}$), defined as the sum of the SFRs of the individual gas particles, calculated based on their gas densities and the assumed sub-resolution star formation prescription; the separation between the nuclei of the interacting pair ($d_{\rm BH}$); and the mass of all stars formed from the start of the simulation ($m_{\rm N}$).

For the radiative transfer, the Milky Way $R = 3.1$

TABLE 1
Observed galaxies

Galaxy	Type	α	δ	z
NGC 2976	Local merger	09 47 16.3	+67 54 52.0	0.0009
NGC 3031	Local merger	09 55 33.2	+69 03 57.9	0.0009
NGC 3034	Local merger	09 55 52.2	+69 40 47.8	0.0009
NGC 3185	Local merger	10 17 38.7	+21 41 16.2	0.0053
NGC 3187	Local merger	10 17 48.4	+21 52 30.9	0.0061
NGC 3190	Local merger	10 18 05.7	+21 49 57.0	0.0053
NGC 3395/3396	Local merger	10 49 50.0	+32 58 55.2	0.0065
NGC 3424	Local merger	10 51 46.9	+32 54 04.1	0.0061
NGC 3430	Local merger	10 52 11.5	+32 57 05.0	0.0062
NGC 3448	Local merger	10 54 38.7	+54 18 21.0	0.0057
UGC 6016	Local merger	10 54 13.4	+54 17 15.5	0.0064
NGC 3690/IC694	Local merger	11 28 31.2	+58 33 46.7	0.0112
NGC 3786	Local merger	11 39 42.5	+31 54 34.2	0.0097
NGC 3788	Local merger	11 39 44.6	+31 55 54.3	0.0085
NGC 4038/4039	Local merger	12 01 53.9	18 52 34.8	0.0062
NGC 4618	Local merger	12 41 32.8	+41 08 44.4	0.0017
NGC 4625	Local merger	12 41 52.6	+41 16 20.6	0.0019
NGC 4647	Local merger	12 43 32.6	+11 34 53.9	0.0039
M 51a	Local merger	13 29 54.1	+47 11 41.2	0.0018
M 51b	Local merger	13 29 59.7	+47 15 58.5	0.0018
NGC 5394	Local merger	13 58 33.7	+37 27 14.4	0.0131
NGC 5395	Local merger	13 58 37.6	+37 25 41.2	0.0131
M 101	Local merger	14 03 09.8	+54 20 37.3	0.0015
NGC 5474	Local merger	14 05 01.2	+53 39 11.6	0.0014
NGC 2623	Local ULIRG	08 38 24.1	+25 45 16.7	0.0185
UGC 4881	Local ULIRG	09 15 55.5	+44 19 58.2	0.0392
VV 283	Local ULIRG	13 01 50.3	+04 20 00.5	0.0374
Mrk 273	Local ULIRG	13 44 42.1	+55 53 13.2	0.0373
VV 705	Local ULIRG	15 18 06.1	+42 44 44.6	0.0400
NGC 6090	Local ULIRG	16 11 40.4	+52 27 21.5	0.0294
ELAISS	Interm. z ULIRG	00 40 14.6	43 20 10.1	0.265
CDFS2	Interm. z ULIRG	03 28 18.0	27 43 08.0	0.248
CDFS1	Interm. z ULIRG	03 29 04.3	28 47 52.9	0.289
SWIRE4	Interm. z ULIRG	10 32: 37.4	+58 08 46.0	0.251
SWIRE5	Interm. z ULIRG	10 35 57.9	+58 58 46.2	0.366
SWIRE2	Interm. z ULIRG	10 51 13.4	+57 14 26.2	0.362
SWIRE7	Interm. z ULIRG	11 02 05.7	+57 57 40.6	0.550
BOOTES2	Interm. z ULIRG	14 32 34.9	+33:28:32.3	0.250
BOOTES1	Interm. z ULIRG	14 36 31.9	+34 38 29.1	0.354

TABLE 2
Galaxy Models for the simulations

	M0	M1	M2	M3	SMG
M_* (10^{10} M$_\odot$)	0.061	0.38	1.128	4.22	16.0
$M_{\rm tot}$ (10^{10} M$_\odot$)	5.0	20.0	51.0	116.0	940.0
$M_{\rm gas}$ (10^{10} M$_\odot$)	0.035	0.14	0.33	0.80	24.0
$N_{\rm DM}$	30000	50000	80000	12000	60000
$N_{\rm gas}$	10000	20000	30000	50000	48000

dust model from Weingartner & Draine (2001) is used, with the Draine & Li (2007) update. Our treatment of the unresolved structure of the ISM corresponds to the "default" ISM described in L14, which implies that the dust associated with cold clouds is ignored, as opposed to the "alternate" ISM treatment.

4. CHIBURST: A BAYESIAN MONTE-CARLO FITTING ALGORITHM FOR STAR-FORMING GALAXIES

4.1. *SED models*

Our SED fitting method (Chiburst) is based on the original star-forming galaxy SED models described in Dopita et al. (2005, 2006a,b) and Groves et al. (2008). These models compute the SED of a star-forming galaxy as the combination of three main components (each of them accounting for a normalized continuous SFR over different timescales) that can be scaled to adjust the star formation history (SFH) of each galaxy: *(i)* a starburst (ionizing stars + H II regions) population of young stars with a continuous SFR averaged over a period of 10Myr ($\rm SFR_{10}$); *(ii)* a population of stars formed at a constant rate between 10 Myr and 100 Myr ago ($\rm SFR_{100}$); and *(iii)* a component of very recent ($<$ 1 Myr) star formation represented by Ultra-Compact H II regions (UCHIIRs) responsible for dust heating at temperatures of $\sim$300 K ($\rm SFR_1$). In order to model more realistic galaxies, we have used Starburst99 (Leitherer et al. 1999) to compute a fourth component (additional to the Groves et al. (2008) prescription) and included it in our models to account for the population of even older (up to 5 Gyr) field stars, which we parametrize according to their total mass (M_*). This addition extends the range of galaxy types that we can study with the models to include systems where older populations significantly contribute to optical and near-infrared (NIR) wavelengths.

The starburst component comes in two extreme flavors that can be added linearly: a *naked* H II region (stars + atomic gas) and an H II region fully covered by a photon-dominated region (PDR) layer, which is the interface between the ionized gas in the HII region and the molecular gas birth cloud from which the cluster was formed. We interpret their linear combination as a covering fraction of PDR surrounding the H II region ($f_{\rm PDR}$). As thor-

oughly described in Groves et al. (2008), the exact shape of the SED for these two components is controlled by two main parameters: the ISM metallicity and a dimensionless quantity related to the dust heating flux: the compactness parameter ($\mathcal{C}$).

Compactness is a good example of a physical property of individual H II regions that affects the overall shape of the galactic SED. It is related to the total heating flux incident on dust grains located at a certain distance from the ionizing stars. For a spherical expanding H II region, the heating flux is calculated as L/R^2 at each time, where L is the luminosity of the ionizing cluster and R is the radius of the H II region, which in turn depends on the cluster mass and the ISM pressure. Hence, models that preserve the run of dust temperature with time should also preserve the quantity L/R^2 averaged over time:

$$\log \mathcal{C} \propto \frac{< L_*(t) >}{< R(t)^2 >} \tag{1}$$

The compactness parameter is proportional to this ratio, and hence sets the evolution of dust temperature with time. Explicitly, the parameter $\mathcal{C}$ can be written in terms of the average star cluster mass $M_{\rm cl}$, and the average pressure of the ISM (P_0/k) in a given system:

$$\log \mathcal{C} = \frac{3}{5} \log \left(\frac{M_{\rm cl}}{M_\odot} \right) + \frac{2}{5} \log \left(\frac{P_0/k}{\rm cm^{-3}\,K} \right) \tag{2}$$

The main effect of compactness on the galaxy SED is a shift of the peak of FIR emission towards shorter wavelengths for larger values of $\mathcal{C}$. An important remark: as defined here, compactness should not be mistaken for the compactness defined in terms of the projected star formation density (for example in Elbaz et al. 2011), since the latter relates to a global observational property of galaxies, namely the projected star formation density. Nevertheless, one of the goals of this paper is to study any correlation between the two types of compactness.

We have interpolated from the original grid of galaxy SED models to create a continuous parameter space for the star forming parameters described above. Additionally, dust extinction due to diffuse dust in the galactic systems studied (i.e., not associated with H II regions) is also a free parameter in our models, parametrized as the visual extinction in magnitudes (A_v). We use the attenuation law of Fischera & Dopita (2005) that approximates the empirical Calzetti extinction law for starburst galaxies (Calzetti 2001).

4.2. *Fitting*

CHIBURST is a Bayesian Monte Carlo fitting routine to fit multi-wavelength observations of galaxies using the models described above. It takes the galaxy photometry and/or spectroscopy data and their uncertainties as inputs, compares them with the SED models of Groves et al. (2008) with the parametrization described here, and calculates probability distribution functions (PDFs) for the following model parameters: the stellar mass (M_*), $\rm SFR_{10}$, $\rm SFR_{100}$, $\rm SFR_1$, the PDR covering fraction ($f_{\rm PDR}$), the compactness parameter ($\mathcal{C}$), the ISM ambient pressure (P/k_0), the mean metallicity of the system (Z), and the visual extinction in the line of sight towards the system (A_V).

Here is how it works: starting from Bayes's theorem, CHIBURST calculates posterior PDFs for the model parameters as the product of two distributions: the likelihood that the data can be drawn from a particular combination of model parameters, and a prior distribution for the model parameters that accounts for any independent evidence collected on particular observables. The likelihood that a model parameter has a given value is obtained from the distribution of χ^2 for models with that value of the parameter. The posterior PDFs are the most complete solution that we can obtain given the available data, the parameter space of models, and the independent evidence on the parameter values.

4.2.1. *The Probability Distribution Functions*

Suppose that you have obtained photometry of a galaxy in different bands, with certain observational uncertainties associated. Bayes Theorem states that, given those observations, the probability $P(M|D)$ of an SED model M being a true representation of the observed galaxy SED data D, is proportional to the product of the likelihood that your data-points can be obtained from your model ($P(D|M)$) times a prior distribution $P(M)$ that contains independent evidence of certain model parameters having certain values. $P(M|D)$ is what we call the posterior PDF and is the solution we are after. The likelihood $P(D|M)$, or the probability of the data given the model, can be obtained from the distribution of reduced χ^2 values if we assume that the observational errors are Gaussian, i.e., if we assume that multiple measurements of the flux at a particular band will distribute according to a Gaussian. The expression for the likelihood is then:

$$P(D|M) = \sum_i \exp\left(-1/2\,\chi^2_{\rm red,i}\right) \tag{3}$$

where the sum is marginalized for each model parameter over all possible $\chi^2_{\rm red,i}$ values for models with a given value of the parameter. The *prior* $P(M)$ is a measure of any previous knowledge that you have on a particular parameter or set of parameters. For example, if you have reliable independent measurements of the stellar mass in a galaxy then you can constrain the possible solutions to your problem by constructing a prior on ($M_{\rm cl}$) that is compatible with those extinction measurements. In the present work we use uniform priors to specify ranges of reasonable value for our parameters, and to bias our posterior PDFs as less as possible. Finally, you need to apply a normalization factor to your posterior PDF to guarantee that the probability of at least one model being a representation for your galaxy equals one.

4.2.2. *Stepping across the parameter space*

Given the infinite size of the parameter space (we interpolate from the original grid to allow any value of the parameters), it is not possible to calculate the posterior PDF for every single allowed value of the model parameters, especially as more data points are added and additional model parameters are considered. Instead, we use a Monte Carlo Markov Chain (MCMC) approach to step across the parameter space while properly sampling the posterior PDF. The idea is simple and is based on the

Metropolis-Hastings algorithm: we start at a given location of the parameter space where we can calculate the value of $P(M|D)_{\rm old}$ and then randomly move to another location where we calculate the new value of $P(M|D)_{\rm new}$. We then calculate the ratio $P(M|D)_{\rm new}/P(M|D)_{\rm old}$ and compare it to a random number between 0 and 1. If the latter is lower than the calculated ratio, we accept the step and update the value of the model parameters to those of $P(M|D)_{\rm new}$. If, on the other hand, the ratio of probabilities is lower than the random number, we reject the step and the model remains unchanged. If the step size and the number of iterations are properly chosen, this process should converge to the posterior PDF. In other words, the histogram of models selected in this fashion should be a representation of the initially unknown posterior PDF, and tells us where in the parameter space are the most likely solutions located, given all the information at hand. This is the ultimate solution to our fitting problem.

5. RESULTS

We have fitted the multi-wavelength photometry of the simulated interactions described in §3 and the actual observations of interacting systems of §2 using CHIBURST. We have chosen the simulations and the observations to cover a broad range of galactic masses, interactions stages, luminosities and morphologies, so that a comparison between the results for both samples will provide insights about the underlying physics associated to a particular SED shape. In this Section we first describe the fits to the simulated mergers and then we move on to the real observations.

5.1. *Simulated mergers*

We have obtained fits for 720 mock SEDs, each corresponding to a different snapshot for the progenitor isolated galaxies (M0, M1, M2, and M3), their paired interactions, and the SMG simulated merger (Table 2). For the interactions, the snapshots cover the interval between the initial approach, and the moment when they reach a passively evolving stage, after coalescence (between 2.5 Gyr and 6 Gyr, depending on the total mass). A higher time resolution is used near the coalescence phase. In this paper we limit our study of the mock SEDs to a single viewing angle, but further down in this section we briefly explore the effect of viewing angle on the derived parameters.

5.1.1. *Fitting of the mock photometry*

Fig. 1 shows an overview of our SED fitting code at work. Plotted in the lower left corner is $\rm SFR_{inst}$ for the M2-M3 interaction as a function of time, as calculated in our simulation. $\rm SFR_{inst}$ increases during the first passage at around 1 Gyr after the start of the simulation and then increases abruptly during the coalescence phase, at around 3 Gyr. We have indicated three particular times along the interaction sequence that serve as representative stages of the interaction: right after the first passage, at the peak of $\rm SFR_{inst}$, and during the phase after coalescence.

For the selected snapshots, we show the mock SEDs and the corresponding best CHIBURST fits in the insets surrounding the time evolution plot. The most remarkable change in the SED as the interaction evolves is in the relative contribution of FIR emission (coming from the H II regions) to the bolometric luminosity of the system, which peaks during coalescence. The contribution of optical and NIR emission from the oldest field stars remains rather constant along the interaction, whereas the UV emission (to which both the H II regions and the stars formed during the 100 Myr prior to a given snapshot contribute) follows the FIR emission, although it significantly decreases in the relaxation phase after coalescence. A similar behavior is observed in all remaining simulations, with the SEDs of less massive interactions and isolated galaxies evolving much less dramatically than in the strong mergers.

Also shown in the small insets are the PDFs derived for three of the model parameters: log $\mathcal{C}$, $\rm SFR_{10}$, and M_*. The shaded regions in these PDFs correspond to the 1σ (blue) and 90% (red) confidence levels and represent the most general description of the uncertainties involved in the fitting when all possible points of the parameter space are considered. In a few cases, the best-fit values are outside the 90% confidence region, which suggests that they can differ very significantly from the median-likelihood values. Model degeneracies are likely responsible for this behavior.

The 1σ confidence regions estimated from the PDFs are small compared to the parameter allowed ranges (typically a third or a fourth of the range), and therefore we are able to infer actual differences in the parameters between simulations. Take, for example, the SFR over the last ten million years ($\rm SFR_{10}$), as estimated from the contribution of the H II+PDR region to the bolometric SED. Near coalescence, CHIBURST gives a 1σ range for this parameter between $\sim$0.50 and $\sim$0.80 $\rm M_\odot$/yr for the M1-M1, whereas for the M1-M2 interaction the obtained solutions range between 0.30 and 0.65 $\rm M_\odot$/yr. These are two systems with similar masses and star formation histories before coalescence, but despite their similarities, we are able to differentiate their fundamental parameters using our method. Similarly, other parameters such as A_V, $\log\mathcal{C}$, M_*, and $f_{\rm PDR}$ can now be compared from system to system in a statistically meaningful way. Further down, in §5.1.2, we will investigate how the derived PDFs relate to the *a priori* known values that we know from the simulations.

The SED fit plots show how different model parameters control the flux in different wavelength regimes: the UV is dominated by emission from stars younger than 100 Myr, either those associated with the unobscured, youngest and most massive systems in the H II regions and parametrized as $\rm SFR_{10}$ (dashed cyan line), or field A-type stars lasting 10 times longer and parametrized by $\rm SFR_{100}$ (single-dot dashed red line); the optical and near-infrared are dominated by the photospheres of the oldest field stars parametrized by M_* (dashed purple line), whereas the mid-infrared (MIR) and FIR emission comes almost entirely from the H II regions and the PDRs with bright PAH emission (because no heating of diffuse dust from older stellar populations is included in the models), again parametrized by $\rm SFR_{10}$ (the dashed light blue line again). In certain systems, there might be a non-negligible contribution to the MIR from UCHIIRs, parametrized by $\rm SFR_1$ (triple-dot dashed yellow line). The estimation of the total SFRs and stellar mass benefits from a multi-wavelength approach that accounts for

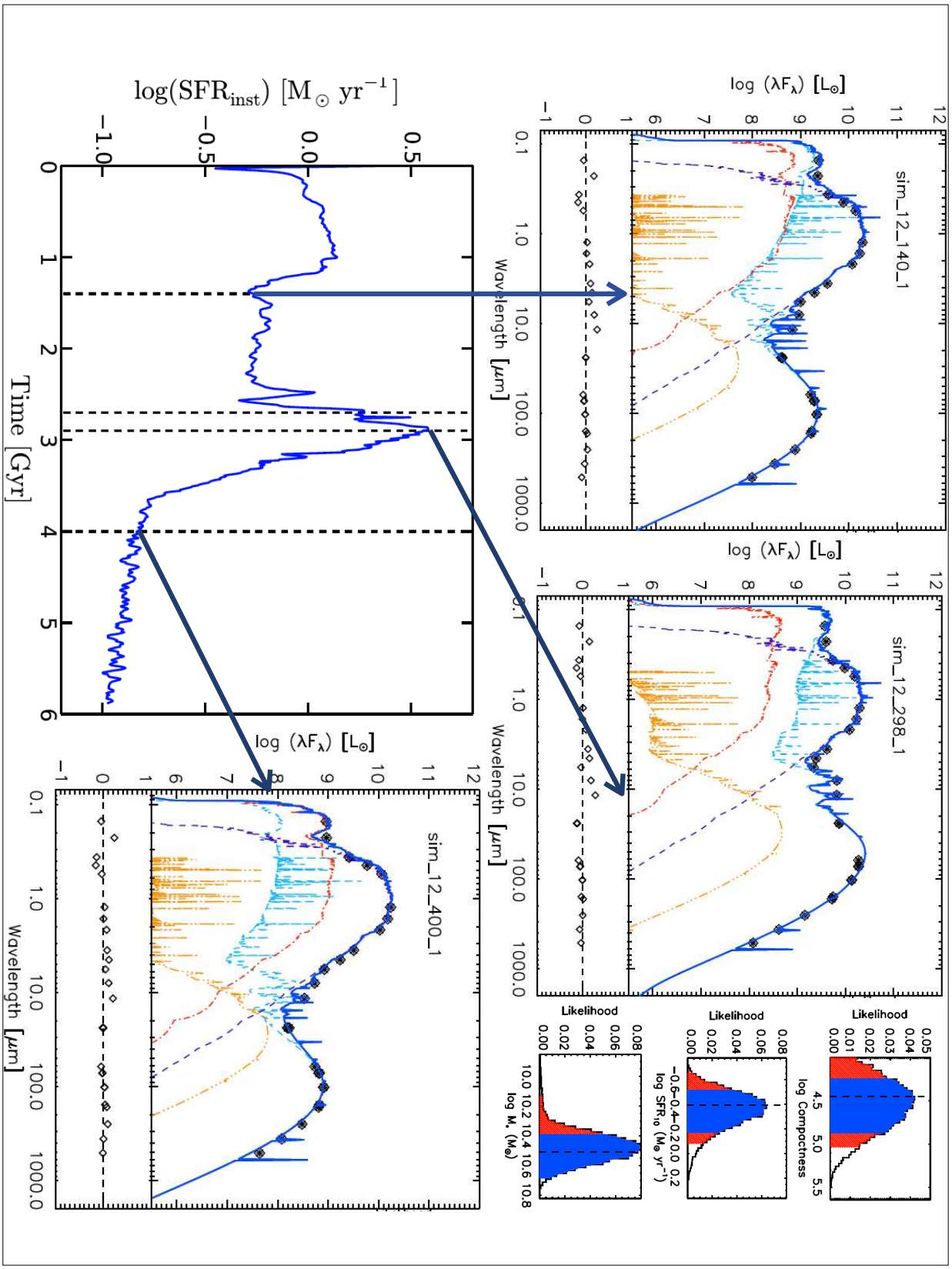

FIG. 1.— The evolution of the SED during the M2-M3 interaction. The instantaneous SFR of the simulation as a function of time is plotted on the lower left corner. The dashed lines indicate particular moments along the interaction. Star formation is enhanced during the first passage at around 1 Gyr and reaches an absolute maximum at coalescence, after about 3 Gyr from the start of the simulation. Also shown are the SEDs for three of the snapshots indicated. Different SED component are color-coded as follows: H II+PDR region (dashed cyan); 10-100 Myr population (single dot-dashed red); UCHIIRs (double dot-dashed yellow); and 5 Gyr population (dashed purple). The panels to the right are examples of the derived PDFs for the model parameters for the 4 Gyr snapshot. Shaded areas corresponding to the 1σ confidence region (blue) and the 90% confidence region (red). The dotted line in each sub-panel corresponds to the best fit values.

both the obscured and unobscured components.

To illustrate how the method works for mergers of different masses, in Figs. 2(a)-2(d) we show fits to the mock SEDs of the simulations corresponding to the interaction pairs M0-M1, M1-M1, M1-M2, and M2-M3, all of which have different total stellar masses. The SEDs shown correspond to a moment of enhanced SFR, near coalescence. Typically, more massive interactions have larger bolometric luminosities, and the relative contribution of FIR (8-1000 μm) emission to the total luminosity tends to increase with the total mass of the interacting galaxies, an early indication that more massive interactions have larger specific SFRs near the coalescence phase.

This is however not always the case. The M1-M1 interaction, for example, has a larger FIR contribution at coalescence than the M1-M2 system, which is more massive. In fact, our results show that the largest fractional FIR luminosities happen preferentially in interacting pairs where both galaxies have equal (or similar) masses. This occurs because, all else being equal, the strength of the starburst induced by a merger decreases as the mass ratio between the progenitors increases (Cox et al. 2008). There is also a trend for the FIR bump peaking at shorter wavelengths in those systems where the FIR emission is larger (see also Hayward et al. 2012). We will later interpret this peak shift in terms of the compactness parameter (Eq. 2), and will argue that this particular SED characteristic reveals an interesting property of the ISM physics in interacting systems.

As discussed in L14 and in Hayward & Smith (2014), the viewing angle mostly affects the SED in the UV bands, where the obscuring effect of dust is larger. At these wavelengths, the typical variations in λF_λ are of the order of 0.25-0.5 dex, and reach a maximum immediately after coalescence, when a large amount of UV photons from young massive stars are absorbed by thick layers of dust. To study the effect of viewing angle on our derived parameters, we have taken the most massive of the original simulations (not including the SMG), corresponding to the M3-M3 merger, and fitted the post-coalescence SED for two different cameras corresponding to orthogonal viewing angles. Fig. 3 shows the results of this exercise. We do not see significant changes in the derived PDFs for the parameters, except perhaps for a difference of 0.1 dex in the derived value of $\log A_V$. More relevant for the present study is the fact that differences in viewing angle do not significantly affect the estimation of the compactness parameter or the SFR, because these parameters are better constrained using the MIR and FIR emission, where dust obscuration is negligible or nonexistent. Moreover, we know that in the post-coalescence phase, when the effect of viewing angle is more important, the infrared indicators significantly overestimate the SFR (Calzetti et al. 2010; Hayward et al. 2014), and so we interpret the post-coalescence parameters with caution.

5.1.2. *Validating the method: true physical parameters vs. derived parameters*

To validate the results of applying CHIBURST to real observations, we first compare the relevant parameters derived from the fitting of mock SEDs with the *true* values from the hydrodynamical simulations. In the latter, unresolved star formation is accounted for by assuming that gas particles with densities above certain threshold form stars according to the volume-density-dependent Schmidt-Kennicut law. The resulting star particles are assigned STARBURST99 SEDs with a Kroupa initial mass function (IMF), which are the input for the radiative transfer code. Since CHIBURST assumes the same IMF, we assume the *true* SFR to be the instantaneous SFR from the simulations, as defined above. In Fig. 4(a) we show the correlation between $\mathrm{SFR_{inst}}$ and the CHIBURST-derived value of $\mathrm{SFR_{10}}$.

CHIBURST overestimates the instantaneous SFRs, but not dramatically: for the most massive interactions (M2-M3, M3-M3), we obtain SFRs that are an average factor of 2 above the true values, whereas for the less massive systems $\mathrm{SFR_{inst}}$ and $\mathrm{SFR_{10}}$ are in good agreement within the 1σ uncertainties derived from the PDFs. The outliers of this correlation, significantly above the majority of points (up to a factor of 100), correspond to the post-coalescence phase of the most massive mergers, where star formation is abruptly quenched. One possible reason for the post-coalescence overestimation of the SFR is heating from stellar populations older than 10 Myr (Hayward et al. 2014), which is not accounted for in the models. When dust heating from stellar populations is included in the SED modeling, the SFR can be recovered much more accurately in the post-coalescence phase (Hayward & Smith 2014). This effect is much more important after coalescence, when the fraction of recently formed stars decreases dramatically. Note that the correlation spans over a range of 3 orders of magnitude in $\mathrm{SFR_{inst}}$. The SMG simulation is also in good agreement with this correlation, which indicates that CHIBURST can determine the true values of SFR within a factor of 2 over a dynamic range covering almost five orders of magnitude.

We also compare the stellar mass present in each simulation with our estimation of the M_* parameter from CHIBURST. In Fig. 4(b) we show this comparison for the original L14 simulations. We slightly underestimate the total stellar mass, obtained by summing up the initial disk and bulge stellar masses, and the mass of stars formed during the simulation. We obtain stellar masses that are a factor of 1.25 or less below the true stellar masses, with better agreement near the coalescence phase. The combined effect of slightly overestimating the SFR and underestimated the stellar mass implies that our derived values for the specific SFR ($\mathrm{sSFR} \equiv \mathrm{SFR_{inst}/M_*}$) are within a factor of 2.5 (or 0.4 dex) of the true values. In general, the uncertainty in the determination of the sSFR is method-dependent. By collecting published values of the sSFR as a function of stellar mass and redshift using various methods, Behroozi et al. (2013) have estimated the uncertainty in sSFR due to the use of different techniques to estimate it. They show that such uncertainty varies from 0.3 dex to 0.4 dex for stellar masses between $10^{10.5}$ $\mathrm{M_\odot}$ and $10^{9.5}$ $\mathrm{M_\odot}$. Our derived values for sSFR are therefore within the uncertainty associated with the use of a particular method.

5.1.3. *PDR covering fraction and extinction*

Extinction due to interstellar dust affects the emission at UV and optical bands. At these wavelengths, radiation is either scattered or absorbed by the dust particles and, if absorbed, re-emitted at MIR and FIR wave-

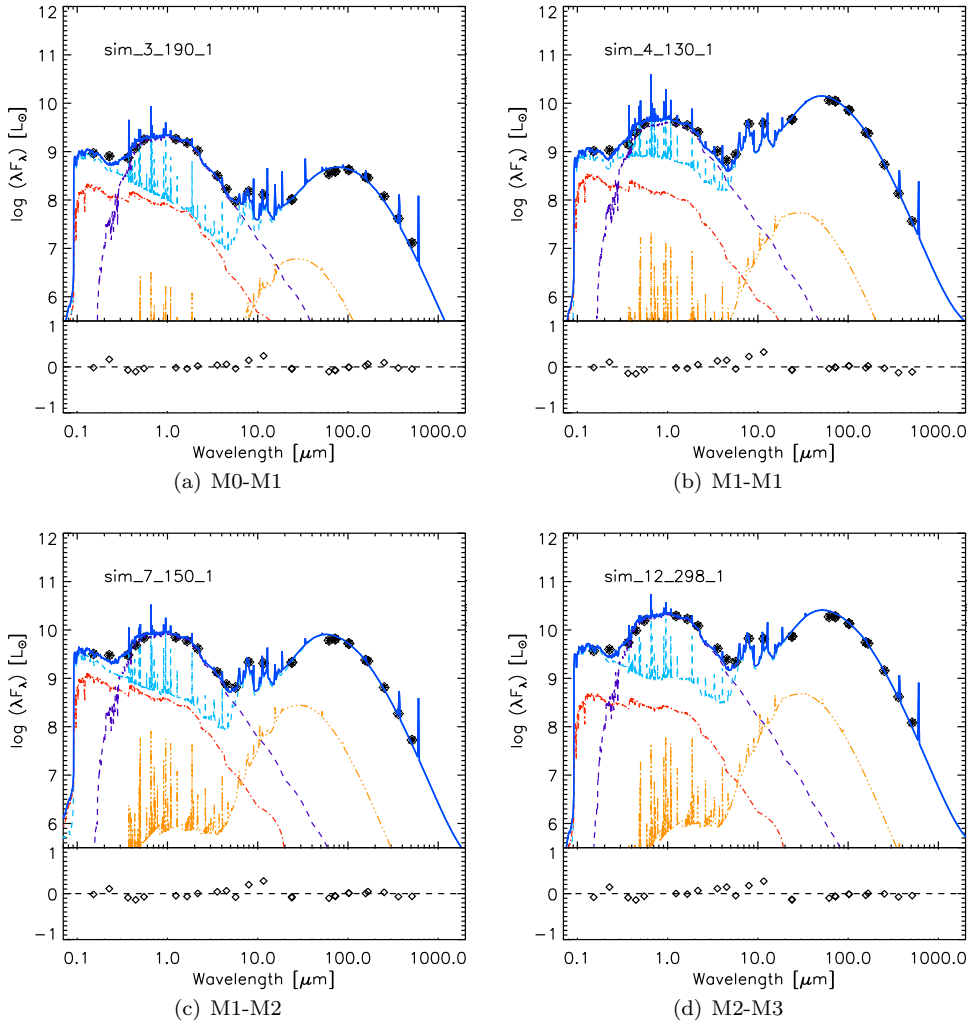

(a) M0-M1 (b) M1-M1

(c) M1-M2 (d) M2-M3

FIG. 2.— Fitted SEDs of four galactic interactions during coalescence, corresponding to the following pairs: *(a)* M0-M1, *(b)* M1-M1, *(c)* M1-M2, and *(d)* M2-M3. The photometric data are shown as black diamonds and the best fit with CHIBURST is shown as the blue line. Lines and color code is the same as in Fig. 1.

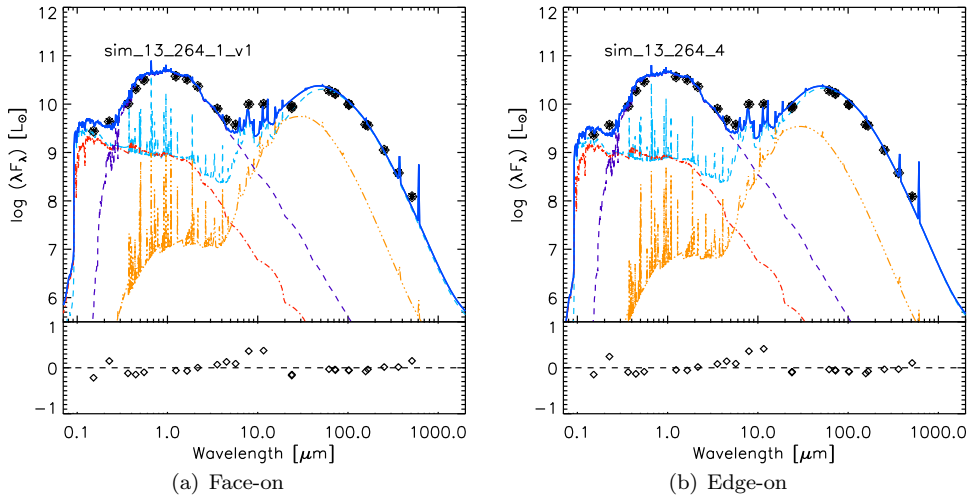

(a) Face-on (b) Edge-on

FIG. 3.— The effect of viewing angle on the SED fitting. Shown is the SED for the M3-M3 interaction right after coalescence, as viewed from two different orthogonal angles.

lengths. In regions heavily enshrouded by dust this effect can be quite significant. The amount of attenuation

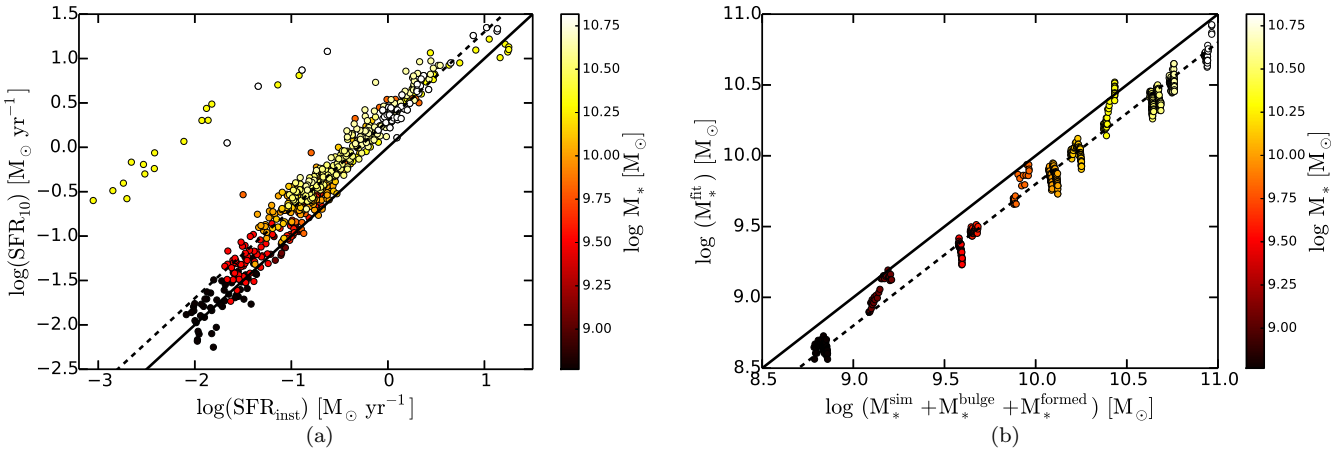

FIG. 4.— *(a)* Comparison between the instantaneous $\mathrm{SFR_{inst}}$ (from the hydrodynamical simulations) and the CHIBURST derived values of $\mathrm{SFR_{10}}$ (peak of the PDF), for the complete set of the L14 simulations (including isolated galaxies and mergers). The solid line indicates the one-to-one correlation, whereas the dashed line is shifted upwards by a factor of 2. *(b)* Comparison between the total stellar mass in each simulation (including initial disk and bulge masses and the mass of stars formed from the beginning of the simulation) and the estimated parameter M_* from CHIBURST (peak of the PDF). The solid line indicates the one-to-one correlation, whereas the dashed line is shifted downwards by a factor of 1.25. In both panels, the points are color-coded by total stellar mass.

at each wavelength follows a wavelength-dependent attenuation curve which is characterized in terms of the V-band attenuation in visual magnitudes, A_V. As discussed in Groves et al. (2008), the H II regions plus PDRs only reach a maximum A_V of 0.8 for a solar metallicity starburst. Additional extinction due to foreground diffuse dust needs to be accounted for in order to correctly describe the extinction in luminous ULIRGs. CHIBURST allows for this additional extinction (A_V) to be a free parameter of the fitting. The attenuation curve used is that described in Fischera & Dopita (2005), corresponding to a turbulent foreground screen. This curve shows decreasing extinction with wavelength, and three main absorption features: two silicate features at 10 μm and 18 μm, and a weaker absorption feature at 0.2 μm due to the carbon ring π-orbital resonance.

In Fig. 5 we show show a plot of $\log \mathcal{C}$ as a function of $\log$ sSFR color-coded by the amount of A_V required in each case (left panel) and covering fraction of PDRs (right panel) for all snapshots in all the original L14 simulations. Extinction values range from $\log A_V \sim -0.8$ to $\log A_V \sim 0.5$, with a median value of $\log A_V = 0.0$ and a standard deviation (in logarithmic scale) of 0.3. We do not detect a strong trend between A_V and compactness, but the highest extinction values ($A_V \sim 3$) are required to fit massive systems near coalescence. This general behavior could be attributed to a screening effect: we only see optical and UV radiation emitted near the skin of the obscuring material and only near coalescence, when most of the starlight is being processed by dust, do we see an effect of the obscuration. The distribution of PDR covering fractions is more uniform, with a median value of 60% and a standard deviation of 14%. In this case, however, we see a smooth evolution of the PDR covering fraction with compactness, with early stage interactions having low covering fractions ($f_{\rm PDR} \sim 40\% - 50\%$) and strong late mergers having almost 100% covering fraction of PDR. Such behavior is expected if PDRs trace recent star formation and are therefore enhanced in the most active phases of the starburst.

5.1.4. *Age of the starburst*

During a starburst episode, most of the UV radiation in emitted by young (< 10 Myr), massive stars. Shortly after a starburst ends, H II regions that are initially fully covered by star formation-induced PDRs start to dissipate, due to mechanical and radiative pressure exerted by the youngest stars. Also, stellar populations start to age, which means that at these post-starburst stages a considerable amount of the observed UV emission arises from older (> 10 Myr) field stars that have dissipated their surrounding ISM but that are still emitting significant amounts of UV photons. In absence of additional attenuation by foreground dust, these photons reach us directly without having been processed by the ISM. This means that a good empirical way to estimate the time that has passed since a starburst is by comparing the amount of UV emission originating in the 10 Myr population with that originating in older (up to 100 Myr) stars. We can do this using our models by comparing the ratio $\mathrm{SFR_{10}/SFR_{100}}$. Systems with a recent starburst event should have higher values of this ratio.

In Fig. 6 we plot $\mathrm{SFR_{10}/SFR_{100}}$ for each snapshot of the simulations against the gas depletion time $\tau_{\rm d}$, that we obtain by dividing the gas mass remaining in each snapshot by our estimated value of $\mathrm{SFR_{10}}$. We have excluded the isolated systems from the plot, because they do not show a strong evolution of star formation with time as in the case of interactions. The ratio is related to the recent SFH at a given snapshot: $\log(\mathrm{SFR_{10}/SFR_{100}}) \sim 0$ corresponds to systems where $\mathrm{SFR_{inst}}$ has remained constant over periods of at least 100 Myr. For example at around 2 Gyr after the start of the simulation in Fig. 1 (no ongoing starburst); $\log(\mathrm{SFR_{10}/SFR_{100}}) > 0$ correspond to systems where $\mathrm{SFR_{inst}}$ is increasing, with larger ratios for steeper increases, such as in the most massive interactions near coalescence in Fig. 1. Finally, systems where $\log(\mathrm{SFR_{10}/SFR_{100}})$ is significantly below 0 correspond to post-starburst systems, where $\mathrm{SFR_{inst}}$ is rapidly decreasing. In Fig. 6, the dashed line corresponds to the following one-to-one correlation:

$$\log \tau_{\rm d} = -\log\left(\frac{\mathrm{SFR_{10}}}{\mathrm{SFR_{100}}}\right) + 9.75 \qquad (4)$$

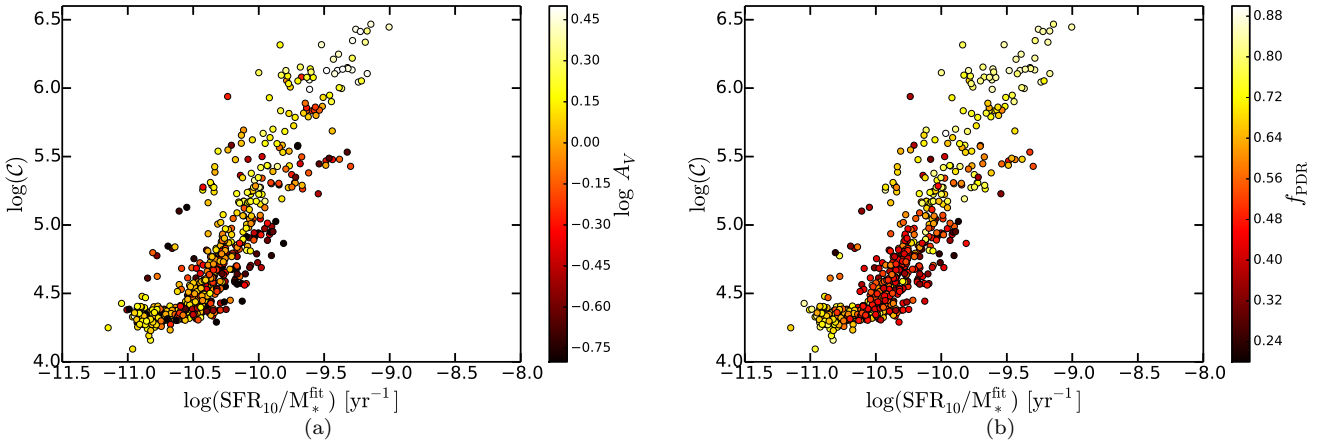

FIG. 5.— *(a):* The log sSFR-log $\mathcal{C}$ diagram for the original L14 simulations color coded by extinction value (A_V). *(b):* The log sSFR-log $\mathcal{C}$ diagram for the original L14 simulations color coded by covering fraction of PDRs ($f_{\rm PDR}$). All values shown correspond to the peak values of the PDFs.

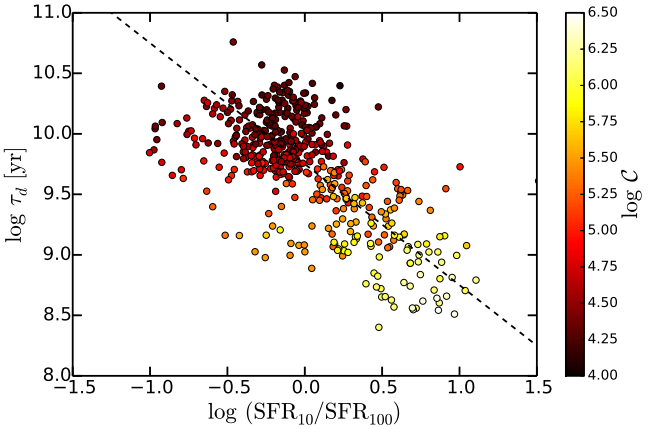

FIG. 6.— Correlation between the age of the starburst, parametrized as the ratio between young (< 10 Myr) and old (100 Myr) populations, and the gas depletion time $\tau_{\rm d}$, for the original L14 simulations along the full duration of the interactions. The circles are color coded according to their compactness, and the dashed line corresponds to the one-to-one relation of Eq. 4.

Fig. 6 indicates that there is an evolution of the gas depletion timescale as a function of interaction stage. This implies that star formation is much more efficient near the peak of the $\rm SFR_{10}/SFR_{100}$ than in periods of secular star-formation, when the SFR is constant over larger time intervals. This is an expected effect in the merger paradigm: star formation efficiency increases as a consequence of the fast collapse of as into the nuclear regions of mergers. In fact, starbursts are often defined as systems whose gas depletion time is much shorter than the Hubble time. The gas depletion timescale $\tau_{\rm d}$ also correlates with log $\mathcal{C}$. Compactness can therefore be used as a probe of the interaction stage and gas depletion efficiency.

5.2. *Observed galaxies*

Fits to the observed photometry for local mergers, local late-type luminous mergers and intermediate redshift ULIRGs have been performed with the same method as for the simulated mergers. For most of the observed systems, the wavelength coverage is similar as for the mock photometry of the simulations, although some of the bands are missing for specific galaxies. The intermediate redshift ULIRGs appear heavily obscured, and therefore no *GALEX* detections are available. Nevertheless, for these systems the rest-frame UV emission that for local systems falls within the *GALEX* bands starts shifting into the optical, making the lack of *GALEX* data a less severe problem for our purposes.

In Fig. 7 we show example fits for our three groups of galaxies. We are able to obtain good fits over the entire wavelength range (i.e., average residuals are within ±0.2 dex) for most of the observed galaxies. Exceptions include galaxies with a flat, featureless MIR spectrum, such as BOOTES1. Our hydrodynamical simulations, as well observational evidence from IRS observations of embedded active nuclei (Imanishi et al. 2007), suggest that such flat spectrum is due to a significant contribution from mid-infrared AGN thermal emission to the bolometric luminosity (Snyder et al. 2013, Rosenthal et al., in preparation). AGN emission does not significantly affect the galaxy derived parameters for our range of galaxy masses. If that were the case, more significant deviations should be observed in Fig. 4 between true and estimated values, since we would interpret AGN emission as the effect of additional star formation. But such effect is not observed. This has also been corroborated using other fitting tools (Hayward & Smith 2014).

Nevertheless, the range of SED shapes that we obtain for our observed galaxies is contained within the range of shapes for the simulated mergers. We can therefore associate particular observations to specific stages of the simulated interaction, via the differences in their physical parameters measured using our SED analysis. Although there are variations in the number of available datapoints and exact wavelength coverage from galaxy to galaxy, the model parameters are constrained with similar uncertainties as for the case of the simulated mergers, as can be noted by comparing the resulting PDFs. In particular, statistically robust differences in the compactness value for different systems can be inferred from our method. Table 3 lists the most relevant parameters (those that are well constrained) for the observed systems.

5.2.1. *Compactness*

To characterize the observed systems, we now compare their derived properties with those of the simulations. A major question driving the present work is whether the

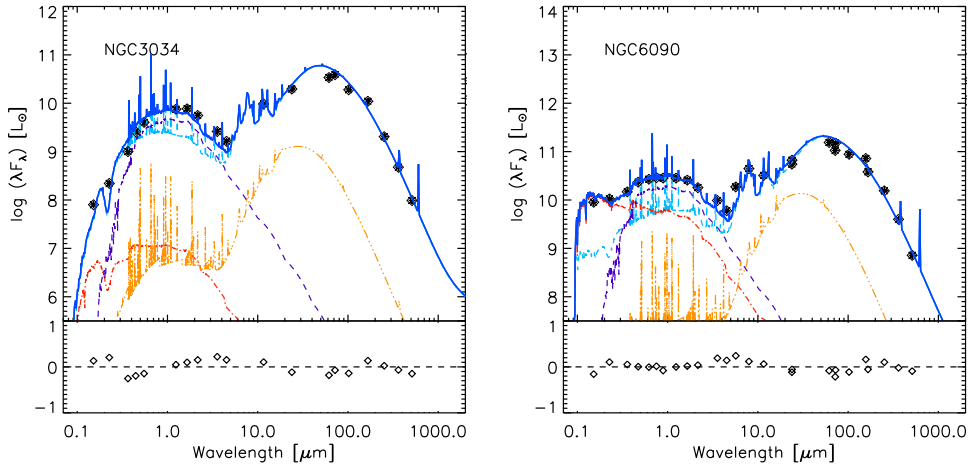

(a) Local merger - M82

(b) Local luminous late-type merger - NGC 6090

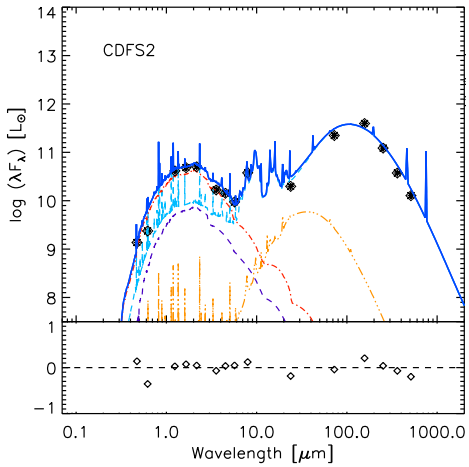

(c) ULIRG at z = 0.248 - CDFS2

FIG. 7.— Example fits for each of our galaxy types. (a): A local merger; (b): A local luminous late-type merger; and (c): A ULIRG at $z = 0.248$. Color code for the different components and PDFs is the same as in Fig. 2.

global star-forming properties of galactic systems, such as the sSFR, relates to the internal physics of the ISM. Another question is whether we can reproduce the star-forming properties of observed luminous systems, both locally and at intermediate redshifts, with models based on interacting systems. The compactness parameter ($\mathcal{C}$) defined earlier is related to the internal conditions of the ISM at the scales of H II regions. It seem therefore a reasonable idea to characterize the systems according to this parameter to see whether we can link compactness to particular stages of the interaction.

Fig. 8(a) summarizes the evolution of $\mathcal{C}$ as a function of star formation activity for all simulated and observed systems in this paper. The plot shows the CHIBURST-derived compactness as a function of the sSFR. The plotted values correspond to the mode of the PDF for each parameter. Included in the plot are: the original M0, M1, M2 and M3 simulated galaxies as well as their paired interactions along the full duration of the simulation, both before coalescence (black circles) and after coalescence (white circles); the SMG simulation at different times during the simulation (large yellow dots); the observed local interactions (red triangles), the stage-4, luminous interactions (that we also call local ULIRGs, blue diamonds), and the intermediate redshift ULIRGs (green squares).

In order to correct for the evolution of the MS with redshift, in Fig. 8(b) we have shifted the intermediate-z galaxies to match the sSFR that they would have in the Local Universe, according to Eq. 13 in Elbaz et al. (2011). This brings them close in the diagram to the local ULIRGs in sSFR. We have fitted straight lines ($\log \mathcal{C} = a \times \log \mathrm{sSFR} + \mathrm{b}$) to the resulting correlation for three different groups of datapoints: the simulations in pre-coalescence stages, the local L13 interacting galaxies[9], and the local and intermediate ULIRGs, excluding the SMG simulation, whose SED evolution we discuss below. In this last group we also include NGC 3690, which is the only of the L13 galaxies with $L_{\mathrm{IR}} > 10^{11}$ L$_\odot$ and has the morphology of a late-type merger. For reasons that will become obvious later, we call members of this last group

[9] Four galaxies have been excluded from the fit: M51b is a post-starburst system where star formation has been quenched (Mentuch Cooper et al. 2012); NGC 3185 and NGC 3190 both belong to the Hickson 44 compact group, and it has been claimed by Alatalo et al. (2014) that suppression of star formation is more likely in such groups; finally, NGC 3031 is an isolated disk more likely to be an analog of the white circles in Fig. 8.

TABLE 3
Fitting results

Galaxy	Type	log SFR_{10} [$M_\odot\,yr^{-1}$]	log SFR_{100} [$M_\odot\,yr^{-1}$]	log M_* [$M_\odot$]	log SFR_1 [$M_\odot\,yr^{-1}$]	F_{PDR}	log $\mathcal{C}$	log A_V [mag]
NGC 2976	Local merger	-0.610	-1.143	9.188	-1.714	0.67	4.88	-0.357
NGC 3031	Local merger	0.008	0.113	10.611	-0.936	0.75	4.36	-0.004
NGC 3034	Local merger	1.007	-1.124	10.154	1.819	0.84	6.04	0.665
NGC 3185	Local merger	-0.120	-0.761	10.073	-0.733	0.81	5.02	-0.057
NGC 3187	Local merger	-0.005	-0.160	9.593	-0.921	0.71	4.72	-0.183
NGC 3190	Local merger	0.263	-1.400	10.652	-0.617	0.92	4.82	0.367
NGC 3395/3396	Local merger	0.848	0.962	10.144	0.154	0.62	5.55	-0.463
NGC 3424	Local merger	0.650	-0.835	10.289	-0.000	0.96	5.54	0.275
NGC 3430	Local merger	0.615	0.355	10.285	-0.749	0.70	5.27	-0.123
NGC 3448	Local merger	0.458	0.232	9.935	-1.035	0.79	5.32	-0.028
UGC 6016	Local merger	-1.414	-0.438	8.140	-2.375	0.82	4.79	-0.722
NGC 3690/IC694	Local merger	2.213	0.622	10.718	1.953	0.95	6.36	0.374
NGC 3786	Local merger	0.382	-0.456	10.331	0.274	0.81	5.17	-0.032
NGC 3788	Local merger	0.271	-0.254	10.239	-0.401	0.81	4.72	-0.263
NGC 4038/4039	Local merger	1.405	0.939	10.888	0.476	0.81	5.49	-0.390
NGC 4618	Local merger	-0.556	0.150	9.300	-1.487	0.83	4.90	-0.768
NGC 4625	Local merger	-0.985	-0.798	8.891	-2.538	0.78	4.98	-0.305
NGC 4647	Local merger	0.320	0.323	10.175	-0.793	0.87	5.28	0.383
M 51a	Local merger	0.869	0.429	10.571	-0.010	0.76	5.14	-0.213
M 51b	Local merger	-0.081	-1.031	10.213	-0.619	0.85	5.10	0.263
NGC 5394	Local merger	1.140	0.346	10.428	1.206	0.90	5.84	0.472
NGC 5395	Local merger	1.204	0.513	11.089	0.298	0.84	4.94	-0.058
M 101	Local merger	0.741	0.847	10.428	-0.107	0.53	4.94	-0.853
NGC 5474	Local merger	-1.129	-0.300	8.976	-1.996	0.81	4.49	-0.843
NGC 2623	Local ULIRG	1.681	0.385	10.352	0.990	0.89	5.70	0.576
UGC 4881	Local ULIRG	1.957	0.361	11.017	0.979	0.95	5.55	0.463
VV 283	Local ULIRG	1.813	0.305	10.702	0.820	0.96	5.77	0.533
Mrk 273	Local ULIRG	2.236	0.559	10.697	1.991	0.96	6.48	0.534
VV 705	Local ULIRG	2.075	0.516	10.861	2.297	0.91	6.13	0.428
NGC 6090	Local ULIRG	1.827	0.240	10.557	1.720	0.86	6.08	0.324
ELAISS	Interm. z ULIRG	2.085	2.319	11.081	1.328	0.80	4.70	1.016
CDFS2	Interm. z ULIRG	2.149	2.278	10.876	1.221	0.85	4.88	1.123
CDFS1	Interm. z ULIRG	2.355	2.201	11.160	1.719	0.82	4.81	0.931
SWIRE4	Interm. z ULIRG	2.250	1.846	10.777	1.360	0.84	5.53	0.756
SWIRE5	Interm. z ULIRG	2.609	1.720	11.590	1.709	0.85	5.21	0.608
SWIRE2	Interm. z ULIRG	2.362	1.703	11.417	1.633	0.82	4.36	1.018
SWIRE7	Interm. z ULIRG	2.879	1.845	11.142	2.146	0.91	5.49	0.464
BOOTES2	Interm. z ULIRG	2.237	1.599	10.893	1.335	0.84	5.28	0.626
BOOTES1	Interm. z ULIRG	3.187	1.671	11.262	3.755	0.84	6.09	0.868

outliers. In Table 4 we list the parameters obtained for these linear fits.

The remarkable correlation between the SFR per unit stellar mass (i.e., the sSFR) and the compactness parameter of Fig. 8 contains valuable information about the MS. This correlation is mostly evident for the simulated systems, holding for all merger masses at all times prior to coalescence. The way this correlation arises in the simulations is through a coupled time evolution of the two quantities: early in the simulation, at secular stages of the SFR, both compactness and sSFR are low. As the merger approaches coalescence, there is a boost of the star formation efficiency, the radiation field intensity increases, and gas compression produces an increase in pressure. Therefore, both compactness and sSFR increase until they reach a maximum at coalescence, and in the process, a galaxy moves along the correlation in Fig. 8. It is easier to visualize this evolution for a single system: in Fig. 9 we show the evolution of sSFR and compactness in time for the particular simulation M2-M2.

All other simulations behave similarly, and they all evolve along the the correlation with slope 1.4. How high the sSFR and log $\mathcal{C}$ of an interacting system can reach along the correlation depends on its total stellar mass, with only the more massive mergers reaching values of log $\mathcal{C}$ above 6.0. In fact, our results show that the largest compactness is achieved in interacting systems with two equal-mass galaxies (e.g., M2-M2, M3-M3). Simulations of isolated galaxies never reach too high in sSFR or compactness, remaining in the lower part of the diagram (log $\mathcal{C} < 5$) and creating the somewhat flatter leg of the correlation seen at the low compactness end. The correlation implies that for a given sSFR, all simulations that reach that particular level of star formation activity have the same compactness regardless of the total mass of the merger.

TABLE 4
Linear fits to the log sSFR-log $\mathcal{C}$ correlation

Group	a	b
Pre-coalescence sims.	1.4 ± 0.1	19.0 ± 0.1
L13 galaxies	1.3 ± 0.2	17.4 ± 0.2
Outliers	1.7 ± 0.3	20.9 ± 0.2

Statistically, the three slopes listed in Table 4 are the same, which implies that a very similar correlation holds for the observed systems as well, and that the simulations correctly describe the observed evolution of compactness. In fact, in both simulations and observations

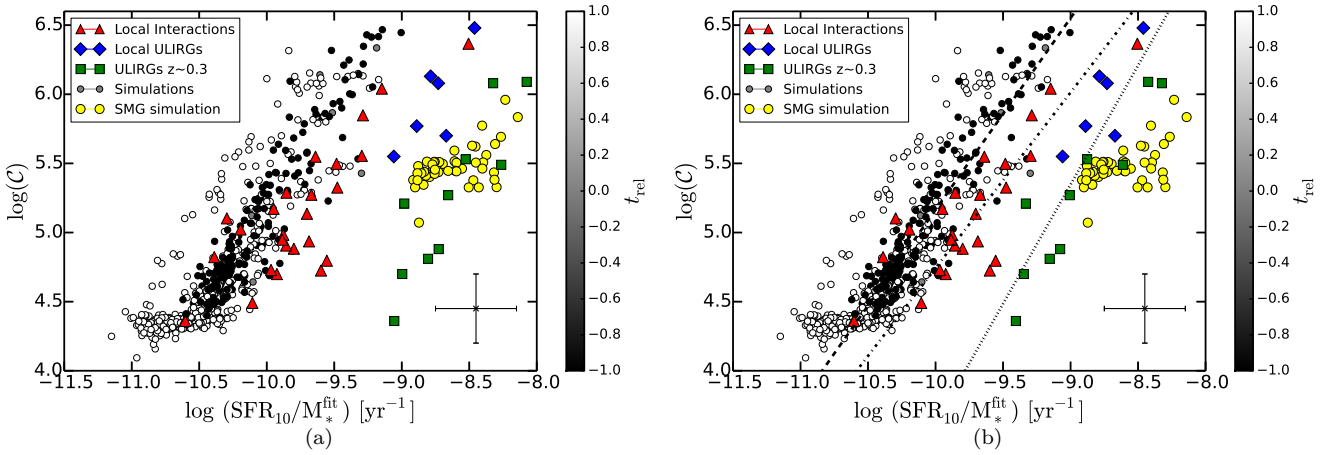

FIG. 8.— (a): The compactness parameter ($\log \mathcal{C}$) plotted against the logarithm of the derived sSFR for all the simulations and observed systems described in this paper. The simulated mergers and isolated galaxies are shown as black (before coalescence) and white (after coalescence) circles. Also shown are the L13 galaxies with available *GALEX* data (red triangles), the local ULIRGs (blue diamonds), and the intermediate redshift ULIRGs (green squares). The SMG simulation is represented by the yellow circles. Typical errors in both axes are indicated in the bottom-right corner. (b) The same plot, but with the intermediate redshift galaxies shifted to match the sSFR that they would have in the Local Universe. Diagonal lines correspond to linear fits to the pre-coalescence simulations (dashed line), the L13 galaxies (dot-dashed line) and the local and intermediate redshift ULIRGs plus NGC 3690 (dotted line). The parameters of each fit are described in the text.

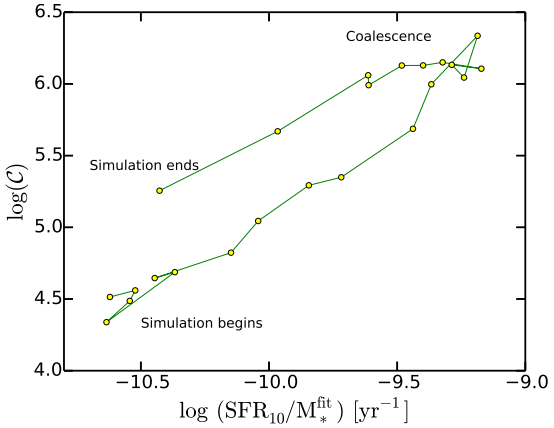

FIG. 9.— The evolution of sSFR and compactness along the timeline of a particular interaction simulation, specifically (M2-M2). Yellow dots correspond to particular snapshots along the interaction sequence, and the green line indicates time evolution.

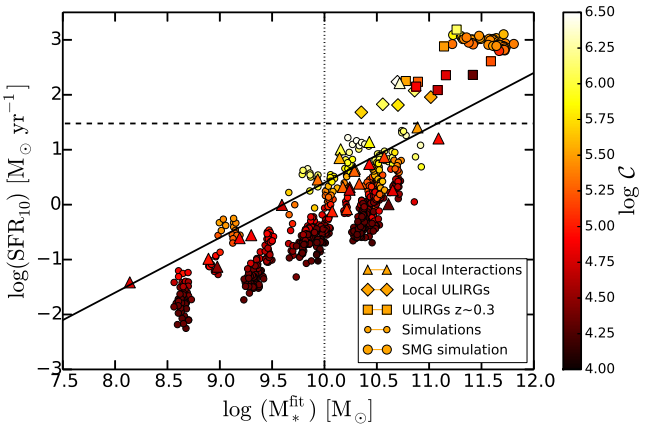

FIG. 10.— The MS of star formation in galaxies as reproduced from our results. The symbols are color-coded by compactness value and represent all simulated and observed systems in this paper, according to the symbols in the legend. The solid line is the fit to the MS in Elbaz et al. (2011). For reference, we indicate the $30\,M_\odot\,yr^{-1}$ limit (dashed horizontal line) and the $10^{10}\,M_\odot$ limit (dotted vertical line).

of local interactions, log $\mathcal{C}$ and sSFR correlate with interaction stage, i.e., observed systems classified as stage 3 or 4 occupy the higher part of the diagram (local ULIRGs included), just like near-coalescence snapshots in the simulations. On the other hand, observed systems with low interaction probability are located in the low compactness end, where the early, pre-coalescence simulated snapshots are located. Nevertheless, the zero-point of the correlation is significantly different for each of the three groups: both the local interactions and the outliers are offset with respect to the simulations, and perhaps more importantly, there is an offset between the local interactions and the outliers. We will discuss the implications of these offsets in § 6.5 in terms of membership to the MS of these systems.

In Fig. 10 we present an alternative visualization of our results that emphasizes the existence of the MS. Shown is the derived SFR as a function of derived M_* for our simulated and observed galaxies, color-coded by compactness value. For the simulated systems, the resulting MS naturally arise as a consequence of the time evolution of star formation in our progenitor galaxies and simulated interactions. In particular, its scatter in the vertical axis, that we measure to be 0.38 dex, is created by the increase in sSFR as systems of different total masses approach coalescence. Systems in near-coalescence stages are closer to the upper envelope of the correlation and also have higher compactness. We note that there is a discrepancy of about 0.4 dex between the locus of our MS and the correlation fitted to local galaxies in Elbaz et al. (2011) (solid line in Fig. 10). As we have mentioned earlier, the determination of the sSFR is method-dependent and the use of different methods between the present work (SED fitting) and that of Elbaz et al. (2011) (conversion from L_{IR} using different SED templates) might account for the difference observed.

Whereas we are not claiming that interactions only are the only cause for the scatter (in fact, at a given time only a small fraction of galaxies is undergoing a merger), our results clearly show that at least some of the

dispersion in sSFR is created by the evolution of mergers, and that the existence of the scatter cannot be attributed to measurement errors only. In other words, the MS is not the result of the majority of galaxies having a single sSFR. Rather, there is a smooth evolution of the sSFR with interaction stage of the mergers, and the observed scatter of the MS with respect to its mean value can be partially understood in terms of this evolution. We note that the presence of mergers ($\sim 20\%$) in the MS has been confirmed by morphological studies of a large sample of galaxies in the COSMOS field (Hung et al. 2013).

The local mergers share the same region of the SFR-M_* parameter space with the simulations, whereas practically all the local and intermediate redshift ULIRGs appear displaced with respect to the MS towards higher sSFR, and have lower values of log $\mathcal{C}$ as expected from their luminosities. It is in this sense that these luminous systems are outliers of the MS, and analogs of the 'starburst mode' galaxies identified in Elbaz et al. (2011). All of these outliers, including the local merger NGC 3690 have SFR above $\sim 30\,M_\odot\,yr^{-1}$, or sSFR above $\sim 7.9\times10^9\,yr^{-1}$, and its condition as outliers of the MS is related to their offset in the sSFR-log $\mathcal{C}$ correlation of Fig. 8. In § 6.5 we study whether all these outliers are compatible with strong mergers (the merger paradigm) or if their internal physical conditions indicate that they might also be pre-coalescence systems.

5.2.2. *The IR8 parameter and its relation to compactness*

In this Subsection we measure the parameter IR8 = $L_{IR}/L_{8\mu m}$ defined in Elbaz et al. (2011) for our set of simulated and observed interactions. The motivation to do so comes from Elbaz et al. (2011), who show evidence that the distribution of IR8 values in star-forming galaxies defines an infrared MS, with the vast majority of galaxies belonging to this MS characterized by a Gaussian distribution of the IR8 value with median IR8 ~ 4. The outliers of this infrared MS ($< 20\%$) form a tail towards larger values of IR8, and have typical IR8 values of 10. They also show that these outliers are systems with compact projected star formation densities. Here we investigate whether we recover a similar distribution of IR8 values from our simulated and observed systems.

We measure IR8 from the best-fitting SEDs obtained with CHIBURST. We integrated the rest-frame SEDs between 8μm and 1000μm to estimate the value of L_{IR} for each system. For observed and simulated systems we then used the (measured or mock) flux density at 8 μm as an estimate of L_8. For those observed systems for which we did not have measured rest-frame 8μm flux densities available, we integrated the SEDs convolved with the IRAC 8μm filter response, in a similar way in which we obtained the mock photometry, and used the resulting value as L_8. We took care in performing the same process for the intermediate-z ULIRGs, using their rest-frame SEDs.

In Fig. 11 we show IR8 as a function of the 8 μm luminosity for all simulated and observed systems, color-coded by value of log $\mathcal{C}$. For the simulated systems (except the SMG simulation), the mean value of the distribution of IR8 values is IR8 = 2 (solid line in the plot), and the standard deviation is 0.12 dex. At all times, the majority of systems are within 1σ of the mean value (indicated by the dashed lines), and outliers include systems with both higher and lower values of IR8, although they are preferentially located in the low-IR8 side of the distribution. No clear indication of a high-IR8 tail can be inferred from these simulated interactions, but all the observed outliers of the MS also appear as outliers of the IR8 distribution, as discussed below.

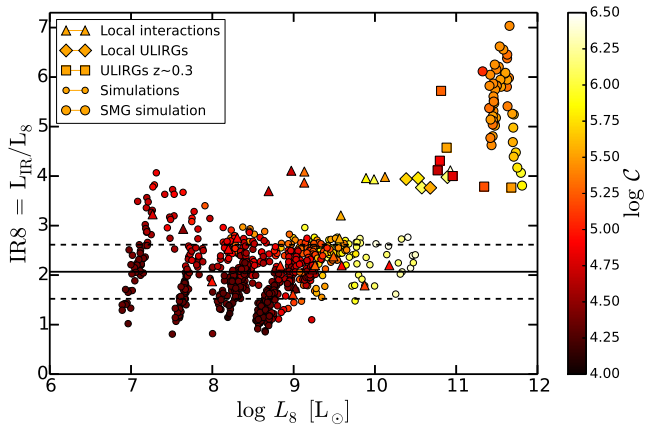

FIG. 11.— The IR8 = $L_{IR}/L_{8\mu m}$ parameter as a function of 8 μm luminosity for simulated and observed systems. The symbols are color-coded according to the compactness of the systems. The solid horizontal line represents the mean value of the IR8 values for the simulated systems, excluding the SMG simulation, whereas the dashed lines mark the 1σ boundaries around the mean.

Objects with high compactness are towards the luminous end of the distribution, and their IR8 values are within the 1σ boundaries. For the observed local interactions (triangles in Fig. 11), the distribution of their IR8 values has a mean of 2.9 and a standard deviation of 0.13 dex, and so they have statistically higher IR8 values than the simulations. The SMG simulation has IR8 values well above the distribution for all the other simulations, with a mean value of IR8 = 5.5. The local and intermediate-z ULIRGs also have IR8 values more than 1σ above the local interactions and the simulations, but still below the values for the SMG simulation, with a mean IR8 value of 4.1 and a small standard deviation of 0.05. With respect to the local observed and simulated mergers, they appear to be members of the high IR8 tail of starbursts reported by Elbaz et al. (2011) in their sample of *Herschel*-selected galaxies.

The mean value of IR8 for the simulated systems in Fig. 11 is a factor of 2 lower than the value reported in Elbaz et al. (2011), for both their local sample of galaxies and the high redshift sample. A number of reasons could explain this disagreement. First, because of the heterogeneous nature of their local sample, both their L_{IR} and L_8 were estimated based on the available photometry, and no homogeneous method was used. In particular, for high-z galaxies, they were relying on SEDs that were usually incomplete in the long-wavelength end, since this part of the spectrum had been redshifted beyond the *Herschel* bands. Finally, they use a different set of SED templates (namely the Chary & Elbaz 2001, templates) to perform the fits to the galaxy photometry. These templates have a similar treatment of the dust particles as our models, but differ in the treatment of the emission from PAHs. Whereas CHIBURST uses an empirical PAH spectrum with optical properties similar to those of coronene, and fitted to two particular interacting galaxies, the Chary & Elbaz (2001) templates use a

mixture of six different planar PAH, and their emissivities are explicitly calculated. All this can have an effect in the measured IR8 values.

6. DISCUSSION

6.1. *General considerations*

We now discuss the implications of our results, and in particular of Figs. 8 and 10. First, for interacting galaxies the so-called local MS of star formation should not be thought of as a one-to-one correlation between SFR and M_*, or equivalently, not all galaxies in the MS have the same SFR per unit stellar mass. Instead, there is a smooth evolution of the sSFR with interaction stage. We interpret the observed scatter of the MS with respect to its mean value in terms of this evolution. Galaxies located near the upper envelope of the MS are systems undergoing mergers near the coalescence phase, with relatively higher sSFR and typical masses of the progenitors exceeding $\mathrm{M}_* = 10^{10}\,\mathrm{M}_\odot$. This evolution is also accompanied by a change in the internal conditions of the ISM as the systems approach coalescence, parametrized by compactness. The ISM in systems near the bottom envelope of the MS is exposed to different environmental conditions than the ISM in high compactness systems. According to the definition of compactness, this translates in different values for the time-averaged ratio of stellar luminosity L_* to spatial extension of the dust R. Both the stellar mass of the starburst clusters and the ISM pressure control this ratio.

Therefore, Fig. 8 implies that the global properties of interacting systems, such as the sSFR or the total luminosity, are linked to the internal properties of the ISM, such as the heating flux incident onto interstellar dust particles in star-forming regions. Galaxies near the upper envelope of the MS do not only have enhanced sSFRs, but they also have warmer distributions of dust temperatures. This cannot be just the effect of the youngest (say younger than 3 Myr) H II regions dominating the FIR SED during the coalescence phase, because compactness, as well as many other star formation indicators, is sensitive to timescales of ~ 10 Myr, (i.e., CHIBURST averages a constant SFH over those 10 Myr for the H II region component), and individual H II region expand much faster. Therefore, a higher $\log \mathcal{C}$ near coalescence must be related to different physical conditions of the ISM. Evidence for variations in the ISM physics across the MS for a given redshift has been collected by several authors (Daddi et al. 2010; Saintonge et al. 2011; Magnelli et al. 2014), although some studies have suggested that the distance from a particular galaxy to the locus of the MS depends only on $f_{\rm gas} = M_{\rm gas}/M_*$ (Magdis et al. 2012). Our results here help to settle this issue.

The second implication has to do with the bimodal distribution of the zero-point for the $\log$ sSFR-$\log \mathcal{C}$ correlation. Our results show that, after the cosmic evolution of the MS has been taken into account, the membership of a system to the MS can be decided based on which of the two different normalizations it belongs to, and not necessarily on its level of starburstiness. The bimodality should be explained in terms of one or several of three possibilities: differences in relative gas content ($f_{\rm gas}$) which would yield higher sSFRs in gas-rich systems; a difference in the efficiency of gas conversion into stars (both of these two options would normalize the correlation of Fig, 8 along the sSFR axis); or a difference in the ISM conditions near the star-forming regions, that would lead to compactness variations, normalizing the correlation along the $\log \mathcal{C}$ axis.

An additional consideration has to do with an incomplete treatment of the ISM physics in the hydrodynamical simulations: the GADGET-3 simulations do not resolve the ISM at the scales of individual H II regions and, although the effective equation of state used in the simulations implicitly includes the effects of supernova feedback, it does not account for the mechanical feedback exerted by radiation from massive stars. Assuming a typical cluster mass of $10^5\,\mathrm{M}_\odot$, then we require variations in $\log(P_0/k)$ between $3\,\mathrm{K\,cm^{-3}}$ and $8\,\mathrm{K\,cm^{-3}}$ to account for the observed variation in compactness. It is likely that differences in the treatment of feedback between the GADGET-3 simulations (that assumes the feedback comes from supernovae) and CHIBURST (that include the mechanical luminosity of a mass-loss bubble) explain the the vertical offset of ~ 0.5 dex between the simulations and the local mergers in Fig. 8.

6.2. *The slope of the* $\log$ *sSFR-*$\log \mathcal{C}$ *correlation*

Let us attempt an interpretation for the slope of the correlation in Fig. 8. Let us start with the fundamental definition of compactness in Eq. 1, and let us assume that the proportionality holds for all times. The amount of luminosity being produced in a patch of ISM scales linearly with the sSFR within that particular patch, and hence:

$$\log \mathcal{C} = \log\ \mathrm{sSFR} - 2 \log\ \mathrm{R} + \mathrm{constant}. \qquad (5)$$

Now, we have already estimated the slope of the correlation to be ~ 1.4. Therefore we have:

$$\log \mathcal{C} = 1.4\ \log\ \mathrm{sSFR} + \mathrm{constant}. \qquad (6)$$

If we compare eqs. 5 and 6, then we can infer that if $\mathrm{sSFR} \propto \mathrm{R}^{-0.25}$, then we recover the measured slope of 1.4 for the $\log$ sSFR-$\log \mathcal{C}$ correlation. A possible interpretation for this is that systems with high sSFR have smaller physical sizes. For a fixed gas mass, the volumetric Kennicutt-Schimdt relation implies a similar effect, i.e., that the specific SFR should be inversely proportional to the volume of the region in consideration. Qualitatively, this is also consistent with observations of local ULIRGs. For example, approximately half of the luminosity of Arp 220 is emitted from within its central 100 pc, which means that this object with very high sSFR is also very compact. Elbaz et al. (2011) also attribute more compact projected star formation densities to their outliers, which they interpret to be starburst.

This interpretation has a flaw: the fundamental definition of compactness in Eq. 1 is referred to the luminosities and physical sizes of individual H II regions. Whereas the "single H II region" interpretation might prove useful for physically compact objects such as Arp 220, it is not straightforward to apply the same description to other geometries of the starburst. Ideally, it would be desirable to relate the slope of the $\log$ sSFR-$\log \mathcal{C}$ correlation to the properties of the ISM that control compactness, i.e., the cluster mass ($M_{\rm cl}$) and the ambient pressure of

the ISM (P_0/k). In the following we provide such an alternative interpretation.

If we assume a standard polytopic equation of state for the gas, we can write:

$$P \propto n_g^{\gamma} \Rightarrow \log P = \gamma \log n_g + \text{constant}. \quad (7)$$

The volume-density-dependent K-S relationship implies:

$$\dot{\rho}_* \propto n_g^{\alpha}, \qquad \alpha \sim 1.5 \quad (8)$$

Thus,

$$\frac{\text{SFR}}{V} \propto n_g^{\alpha}, \quad (9)$$

which after some algebraic manipulation (dividing and multiplying the left side by M_*) implies:

$$\alpha \ \log \ n_g - \log \ \rho_* + constant \quad (10)$$

Combining eqs. 7 and 10, we get:

$$\log \ P = \frac{\gamma}{\alpha}(\log \ \text{sSFR} + \log \ \rho_*) + \text{constant} \quad (11)$$

Now, if we neglect variations in $M_{\rm cl}$ in Eq. 2, the the above equation implies:

$$\log \ \mathcal{C} = \frac{2\gamma}{5\alpha}(\log \ \text{sSFR} + \log \ \rho_*) + \text{constant} \quad (12)$$

Star formation models by Springel & Hernquist (2003) show that reasonable polytropic indexes for the ISM are between $\gamma = 0.75$ and $\gamma = 2.3$. In order to get γ within this range, then we need to assume that the stellar density scales approximately linearly with the sSFR.

Alternatively, we can assume that $M_{\rm cl} \propto n_g^{\beta}$. Using the full version of 2, this implies:

$$\log \ \mathcal{C} = \frac{2\gamma}{5\alpha}(\log \ \text{sSFR} + \log \ \rho_*) + \frac{3\beta}{5\alpha}(\log \ \text{sSFR} + \log \ \rho_*) + \text{constant} \quad (13)$$

With our adopted value of α, reasonable values of γ imply that β should have values between 2 and 3. With the approach that we have just presented, and assuming invariance of the stellar content per unit volume, our results imply that the stellar cluster mass should scale as a power law of the gas mass n_g in star-forming regions.

6.3. *SFR efficiency and gas depletion times*

The gas depletion timescale $\tau_{\rm d}$, which is a measure of the star formation efficiency, varies from system to system along the log sSFR-log $\mathcal{C}$ correlation, and systems in the upper part of the diagram have on average shorter depletion timescales (or larger star formation efficiencies), as indicated in Fig. 6. Using a similar argument, Magnelli et al. (2014) argue that the variations of $T_{\rm dust}$ with $\Delta \log(\text{sSFR})_{\rm MS}$, the distance of a system to the fiducial MS, are related to variations in the gas depletion efficiency. They link this result to observational evidence in local galaxies.

Using atomic and molecular gas observations for a sample of local star-forming galaxies, Saintonge et al. (2011) show evidence for variations in both the gas depletion time $\tau_{\rm d}$ and the gas fraction as a function of distance from the fiducial MS: galaxies above the fiducial MS have higher gas fraction and shorter $\tau_{\rm d}$. They also show that systems that are morphologically more disturbed are those with shorter gas depletion times. In our approach (Fig. 6), variations in $\tau_{\rm d}$ arise as the natural consequence of the evolution of interacting systems as they consume their gas to fuel the intense star formation events during the coalescence phase, when the gas depletion becomes more efficient and the compactness increases. These efficient, compact stages of star formation in mergers are also characterized by a larger contribution from young (< 10 Myr) stars to the bolometric luminosity. We can estimate the depletion time for a particular merger in the local Universe using Eq. 4, or alternatively, from measuring the SED compactness, even if we lack information about the total gas content of the system.

6.4. *Implications for the Main Sequence*

We have seen that the time evolution of our simulated interactions naturally produces something very similar to the measured MS in the SFR-M_* plane, and that the majority of our local mergers fall within this MS, unlike the local and intermediate redshift ULIRGs, that appear as outliers (Fig. 10). According to the merger paradigm, the separation between on- and off-MS systems is explained by the fact that MS systems are disk galaxies that form stars in a time scales that are long, whereas outliers are merger-driven starbursts where star formation happens in timescales comparable to the dynamical timescale of the hosts. Based on morphological studies of a large sample of galaxies with z up to 2.5, Wuyts et al. (2011) find that a majority of galaxies in the MS show a disk-like morphology, which supports this scenario. Several studies, however, have found a significant population of mergers (up to 20%) on the MS (Kartaltepe et al. 2012; Hung et al. 2013). It is therefore important to quantify to which extent mergers contribute to the scatter of the MS, and to what extent they explain the population of outliers.

The results shown here imply that the scatter in sSFR created by the evolution of mergers (0.38 dex) is compatible with the 1σ scatter of about 0.3 measured in several studies of the MS at various redshifts (Noeske et al. 2007; Elbaz et al. 2007; Rodighiero et al. 2011; Whitaker et al. 2012; Schreiber et al. 2014). This does not mean that mergers only are responsible from the scatter. In fact, we have mentioned in the introduction that galaxies spend only a small fraction of their lifetimes as late-type mergers, and that the scatter of the MS could also be related to stochasticity of gas accretion or to variations in the galaxies' star formation histories. What we provide here is a quantification of the merger-driven scatter. Our results also demonstrate that if strong mergers are the cause for a population of MS outliers, they must have masses above 10^11 $M_\odot$, because none of our simulations (except for the SMG galaxy, which is also very gas rich) reaches far above the MS, not even during the coalescence phase. For $f_{\rm gas} > 0.6$, galaxies lie significantly above the MS, but as we have discussed, there seems to be other mechanisms that contribute to the existence of

an outlier population.

In our approach, the correlation between the average dust temperature $T_{\rm dust}$ and the sSFR, as well as its direct relation to the scatter of the MS is explained by the increase of compactness as galaxies move closer to the upper envelope, when they approach the coalescence stage of the merger. We argue that the ISM properties parametrized by the compactness parameter change across the MS, and that such changes can be understood in terms of an increasing ISM pressure or average intensity of the radiation field as mergers evolve towards coalescence. By assuming a typical value for the radiation field near the star forming regions in a given system, we have estimated the pressure changes that would explain the scatter of the MS.

Our results also indicate an association between the outliers of the MS, and the outliers of the infrared MS with relatively high values of IR8. (Fig. 11). However, not all of our infrared MS outliers (all of which are observed systems, except for the SMG simulation) have the SED properties attributed to them in (Elbaz et al. 2011). Specifically, some of them (e.g., CDFS1, CDFS2, ELAISS, SWIRE2) have low compactness, which indicate relatively cold dust temperatures, in contraposition to the typical warm dust inferred for the Elbaz et al. (2011) outliers. In fact, the low compactness of these objects is compatible with either isolated galaxies or early stages of an interaction. The SMG simulation has IR8 values that are up to 3 times larger than in the original simulations, which implies that the $f_{\rm gas}$ plays a role in the increased IR8 values. Within the infrared MS, for a given total stellar mass there is a correlation between IR8 and compactness. This could be interpreted as the result of PAH destruction in very compact systems, due to the strong radiation field of the starburst.

6.5. *Possible interpretations of the offsets. Two regimes of star formation?*

We have seen that the physical conditions of the ISM change across the MS as interacting galaxies approach coalescence, producing at least part of the observed dispersion of the MS. We have argued that, if we assume an invariance of the radiation field from cluster to cluster, these changes can be interpreted as variations in the ISM ambient pressure, and that the effect of such variations is to create a correlation between the compactness of the typical H II region in a given galaxy, which depends upon pressure, and the efficiency of gas depletion, that controls the sSFR. This correlation is represented in Fig. 8 and covers the evolution of mergers of different masses as they evolve from their quiescent, disk-like mode into the coalescence phase. We have also argued that a possible interpretation for the slope of the correlation can be put forward in terms of ϵ, the ratio between $\rm SFR_{inst}$ and the gas density $n_{\rm gas}$, which seems to be the same for local mergers and intermediate redshift ULIRGs. However, one particular feature of Fig. 8 remains unexplained: the different normalization constant that needs to be applied to different populations of galaxies in order to obtain a Universal $\log$ sSFR-$\log \mathcal{C}$ correlation.

For the intermediate-z ULIRGs, part of the offset is explained by the evolution of the MS with cosmic time (Noeske et al. 2007; Daddi et al. 2007; Magdis et al. 2010; Elbaz et al. 2011): the MS shifts towards higher sSFR at higher z. Since the gas content of galaxies also increases with z, a possible interpretation of the evolution of the MS is that high-z galaxies form more stars per unit stellar mass because they have more gas available to do so (Combes 2012, and references therein). Whereas in the Local Universe $\rm sSFR_{MS} = 0.08\,Gyr^{-1}$, at $z = 0.3$ $\rm sSFR_{MS} = 0.16\,Gyr^{-1}$. In fact, using the molecular gas mass estimates of Magdis et al. (2014), which are based on gas-to-dust ratio calculations, we find that for our intermediate-z ULIRGs, the typical $f_{\rm gas}$ is about 0.7-0.8 (and as high as 1.1 for SWIRE7, which brings it close to a typical submillimeter galaxy), or about a factor of 3 higher than the value of $f_{\rm gas}$ in the simulations and local mergers, including the luminous stage 4 mergers (Sanders et al. 1991). Using Eq. 13 in Elbaz et al. (2011) for the normalization of the MS with redshift, we find that this cosmological effect would shift the green squares of Fig. 8 at most by 0.3 dex to the left in the sSFR axis, aligning them with the local ULIRGs and NGC 3690. The remaining offset between the local mergers and the local ULIRGs, therefore, cannot be explained as a cosmological effect. We are left with a bimodal behavior of the $\log$ sSFR-$\log \mathcal{C}$ correlation that defines the membership of particular galaxies to the MS. Galaxies in mode 1 are described by the parameters in the second row of Table 4 and belong to the MS, whereas mode 2 galaxies are described by the parameters in the third row of Table 4 and are outliers of the MS.

The sSFRs of outliers are more than 1σ above the mean value for the MS. Yet, their SEDs are not typical of MS outliers: they are consistent with lower compactness values (and in consequence, a colder $T_{\rm dust}$) than we would expect from their sSFR, even after the cosmic evolution of the MS has been accounted for. We argue that the existence of the two modes can not be attributed exclusively to different relative gas content. We base this argument on the fact that the gas content differences that we estimate are not enough to account for the enhanced sSFR in outliers. Neither is the normalization of the MS using Eq. 13 in (Elbaz et al. 2011), as we have seen. In consequence, either outliers are more efficient at converting gas into stars (i.e. they have shorter $\tau_{\rm d}$), which results in a higher sSFR (but their ISM physics are the same as for MS galaxies), or their $\tau_{\rm d}$ is comparable to that of MS galaxies, but their ISM physics are different, resulting in a significant decrease in the compactness of their star-forming regions. Without favoring any of these two scenarios, we now evaluate their implications.

6.5.1. *Depletion time*

In Table 5 we list the gas depletion times for those galaxies in our sample for which we have found molecular gas masses in the literature. In order to estimate $\tau_{\rm d}$ in each case, we have divided the literature gas mass by our derived $\rm SFR_{10}$. Results indicate that $\tau_{\rm d}$ is systematically shorter ($< 10^9$ yr) for outliers, as compared to the depletion times obtained for the bulk of the simulated interactions (see Fig. 6). These outliers are depleting their molecular gas at a rate comparable with that of local interactions near coalescence. For the local ULIRGs and NGC 3690 this is not surprising, since we know that they are stage 4 systems, with extreme morphological disturbances, and most likely in a near-

TABLE 5
Depletion times

Galaxy	Type	log $M_{\rm gas}$ [$M_\odot$]	$\tau_{\rm d}$ [$\times 10^8$ yr]	Reference
M 51	Local merger	9.88	10.18	Rémy-Ruyer et al. (2014)
NGC 3690	Local merger	10.06	0.70	Sanders et al. (1991)
NGC 4625	Local merger	8.0	96.83	Rémy-Ruyer et al. (2014)
NGC 6090	Local ULIRG	10.15	2.10	Sanders et al. (1991)
NGC 2623	Local ULIRG	9.77	1.23	Sanders et al. (1991)
UGC 4881	Local ULIRG	10.46	3.18	Sanders et al. (1991)
BOOTES2	Interm. z ULIRG	10.51 ± 0.20	1.87	Magdis et al. (2014)
CDFS1	Interm. z ULIRG	11.11 ± 0.13	5.69	Magdis et al. (2014)
CDFS2	Interm. z ULIRG	10.77 ± 0.08	4.18	Magdis et al. (2014)
ELAISS	Interm. z ULIRG	10.77 ± 0.17	4.84	Magdis et al. (2014)
SWIRE2	Interm. z ULIRG	11.36 ± 0.11	10.0	Magdis et al. (2014)
SWIRE4	Interm. z ULIRG	10.67 ± 0.09	2.63	Magdis et al. (2014)
SWIRE5	Interm. z ULIRG	10.97 ± 0.12	0.58	Magdis et al. (2014)
SWIRE7	Interm. z ULIRG	11.17 ± 0.22	1.94	Magdis et al. (2014)

coalescence phase. Therefore, for these local ULIRGs we do not find evidence of depletion times that are shorter than those expected from their evolutionary stages.

In the case of the intermediate-z ULIRGs, on the other hand, some of their log $\mathcal{C}$ values are consistent with early, non-disturbed stages of the interaction (or isolated galaxies). Therefore, we would have expected to measure longer $\tau_{\rm d}$ for these systems. We therefore conclude that at least for the case of intermediate-z ULIRGs, a high gas depletion efficiency can provide an explanation for the different zero-point of the log sSFR-log $\mathcal{C}$ correlation. Such larger depletion efficiency in these systems could be related to a larger fraction of dense gas in outliers (Daddi et al. 2010, see, for example).

6.5.2. *Changes in compactness*

An alternative explanation involves different physical conditions of the star-forming ISM in the two modes. In this case, gas depletion times are similar in both modes, but the ISM near star-forming regions in outliers has a lower value of $\mathcal{C}$ (i.e., has a lower pressure or a weaker radiation field) than the ISM in MS galaxies. If we assume that the distribution of cluster masses in an invariant between the two modes, then we can associate the change in compactness to a difference in the ISM pressure for a given sSFR. Specifically, if we again assume a typical cluster mass of $M_{\rm cl} = 10^5\,M_\odot$ in Eq. 2, then a difference of 0.4 dex in compactness (the amount required to make the two modes overlap in Fig. 8) would correspond to a change in pressure of 1 order of magnitude. In other words, for a given sSFR, the ISM pressure would be 10 times higher in MS galaxies than in outliers. Interestingly, 1 order of magnitude is exactly the pressure difference between the present-day disk and the present-day bulge for a Milky Way-like galaxy, according to recent cosmological simulations (Munshi et al. 2014).

If we adopt this scenario, then the two different normalizations of the log sSFR-log $\mathcal{C}$ correlation can be interpreted in terms of two different pressure regimes for star formation: a high-pressure regime for MS galaxies and a low-pressure regime for outliers of the MS. While for both regimes a broad range of compactness values (and therefore of average dust temperatures) are possible, for a given sSFR the lower ISM pressure in outliers results in systematically colder dust temperatures. We note that this stands in contraposition to previous evidence using stacking of GOODS-*Herschel* sources, suggesting that outliers of the MS have hotter distributions of dust temperatures (Elbaz et al. 2011). Although we do not have large number statistics in our sample, we have applied our method to individual rather than stacked galaxies, and our results highlight the existence of at least a few MS outliers with cold SEDs.

The bottom line: if we attribute the existence of two modes exclusively to different star formation efficiencies, then it is natural to associate the outliers of the MS with merger-driven starbursts where the gas consumption times are short compared to the dynamical timescales of the galaxies. This paradigm, which provides an explanation for the increased sSFR in MS outliers, has been broadly adopted by the community. However, here we show evidence that some outliers of the MS have cold SEDs, that in our hydrodynamical models correspond to systems far from coalescence. If this picture stands, then we need to start looking for mechanisms other than mergers to explain the separation of the two modes. Such mechanisms could involve fundamental differences in the internal physics of the ISM.

7. SUMMARY

Over the last decade, a significant amount of evidence has been gathered that suggests the existence of a main sequence (MS) of star formation in galaxies. This MS is expressed in terms of a correlation between the SFR and the stellar mass of the form SFR $\propto M_*^\alpha$ and spans about two orders of magnitude in both quantities. Several ideas have been suggested to explain fundamental properties of the MS, such as its slope, its dispersion, and its evolution with redshift, but no consensus has been reached regarding its true nature, and whether the membership or not of particular galaxies to this MS underlies the existence of two different modes of star formation. Using a statistically robust SED analysis method based on the star-forming galaxy models of Groves et al. (2008), we have consistently analyzed the star-forming properties of a set of hydro-dynamical simulations of mergers and compared them with real observations of local mergers, local luminous ($L > 10^{11}\,L_\odot$) mergers, and intermediate redshift ULIRGs, with the goal of characterizing the MS. We have reached the following conclusions:

1. We have quantified the contribution of mergers to the scatter of the MS at $z = 0$. We measure this

scatter to be 0.38 dex. The sSFR evolves across the MS due to this effect: as galaxies approach coalescence, they move towards the upper envelope of the MS. This means that at a given redshift the MS should not be thought of as a one-to-one correlation between SFR and M_*. Equivalently, not all galaxies in the MS have the same SFR per unit stellar mass. Instead, there is a smooth evolution of the sSFR with the interaction stage of the mergers. The observed scatter across the MS can be understood in terms of this evolution.

2. The sSFR of star-forming galaxies (and hence, their location across the MS) correlates tightly with the internal physics of the ISM in star-forming regions parametrized by the compactness parameter $\mathcal{C}$. This parameter reflects the heating flux incident onto dust particles near H II regions and depends on the mass of the typical star clusters formed ($M_{\rm cl}$) and on the ambient pressure of the ISM (P_0/k). Galaxies near the bottom envelope of the MS (isolated systems and early stage interactions) typically have low sSFR and low compactness, but both quantities increase as mergers go into the coalescence phase and move towards the upper envelope.

3. None of our simulated mergers, except for the gas-rich SMG simulation, lie far above the MS, not even when they reach the coalescence phase. If outliers of the MS are strong starbursts driven by mergers, they must have total stellar masses above $10^{11}\,{\rm M}_\odot$, or have more gas ($f_{\rm gas} > 0.6$). On the other hand, not all of our observed outliers have SEDs compatible with strong mergers, which indicates that other processes might play a role in the emergence of the outlier regime.

4. The compactness variations across the MS, can be the effect of changes on either the average intensity of the radiation field, or the ISM pressure as mergers evolve into coalescence. Assuming that the average radiation field remains constant, and adopting a typical cluster mass of $10^5\,{\rm M}_\odot$, the variations in compactness across the MS correspond to a boost in pressure from $P_0/k = 10^3\,{\rm K\,cm^{-3}}$ near the bottom envelope of the MS to $P_0/k = 10^8\,{\rm K\,cm^{-3}}$ near the upper envelope.

5. The slope of the log sSFR-log $\mathcal{C}$ correlation implies that systems with large sSFR have relatively small physical sizes, according to: $R \propto {\rm sSFR}^{-0.25}$. For a fixed gas mass, the Kennicutt-Schmidt relation implies a similar trend, that is compatible with observations of luminous, compact starbursts like Arp 220. Alternatively, if stellar density does not change with sSFR, then the measured slope implies that the average stellar cluster mass in a system should scale as a power law of the ISM gas density: $M_{\rm cl} \propto n_g^\beta$, with $\beta = 2 - 3$.

6. The normalization of the log sSFR-log $\mathcal{C}$ correlation has a bimodal nature that determines the membership to the MS of individual galaxies. Mode 1 galaxies belong to the MS and all evolve along the same log sSFR-log $\mathcal{C}$ line as they transit into the coalescence phase. Mode 2 galaxies are outliers and evolve along a similar correlation, but significantly offset towards higher sSFR (or lower compactness) with respect to MS galaxies. Not all of the outliers have SEDs compatible with mergers in the coalescence phase.

7. The observed bi-modality has two possible interpretations. The first one is that outliers have different timescales in the gas depletion ($\tau_{\rm d} = M_{\rm gas}/{\rm SFR}$), perhaps due to the extreme conditions in massive mergers and ULIRGs, and/or by their larger fraction of dense molecular gas. The second possibility involves invariance in $\tau_{\rm d}$ between MS objects and outliers, but a difference in the ISM conditions between the two modes: low-pressure star formation for outliers, and more compact star formation for MS galaxies.

The authors would like to thank Dimitra Rigopoulou and Georgios Magdis for providing the photometry for the $z \sim 0.3$ ULIRGs. JRMG, HAS and LL acknowledge partial support from NASA grants NNX12AI55G and NNX10AD68G, and JPL RSA contracts 1369565 and 1369566. This research has made use of NASAs Astrophysics Data System Bibliographic Services. The simulations in this paper were performed on the Odyssey cluster supported by the FAS Research Computing Group at Harvard University.

REFERENCES

Alatalo, K., Appleton, P. N., Lisenfeld, U., et al. 2014, ApJ, 795, 159
Armus, L., Mazzarella, J. M., Evans, A. S., et al. 2009, PASP, 121, 559
Behroozi, P. S., Wechsler, R. H., & Conroy, C. 2013, ApJ, 770, 57
Brinchmann, J., Charlot, S., White, S. D. M., et al. 2004, MNRAS, 351, 1151
Calzetti, D. 2001, PASP, 113, 1449
Calzetti, D., Wu, S.-Y., Hong, S., et al. 2010, ApJ, 714, 1256
Ceverino, D., Dekel, A., & Bournaud, F. 2010, MNRAS, 404, 2151
Chary, R., & Elbaz, D. 2001, ApJ, 556, 562
Combes, F. 2012, in European Physical Journal Web of Conferences, Vol. 19, European Physical Journal Web of Conferences, 8002
Cox, T. J., Jonsson, P., Somerville, R. S., Primack, J. R., & Dekel, A. 2008, MNRAS, 384, 386
Daddi, E., Dickinson, M., Morrison, G., et al. 2007, ApJ, 670, 156
Daddi, E., Elbaz, D., Walter, F., et al. 2010, ApJ, 714, L118
Davé, R., Finlator, K., & Oppenheimer, B. D. 2012, MNRAS, 421, 98
Davé, R., Oppenheimer, B. D., & Finlator, K. 2011, MNRAS, 415, 11
Dekel, A., Zolotov, A., Tweed, D., et al. 2013, MNRAS, 435, 999
Dopita, M. A., Groves, B. A., Fischera, J., et al. 2005, ApJ, 619, 755
Dopita, M. A., Fischera, J., Sutherland, R. S., et al. 2006a, ApJ, 647, 244
—. 2006b, ApJS, 167, 177
Draine, B. T., & Li, A. 2007, ApJ, 657, 810
Dutton, A. A., van den Bosch, F. C., & Dekel, A. 2010, MNRAS, 405, 1690
Elbaz, D., Daddi, E., Le Borgne, D., et al. 2007, A&A, 468, 33

Elbaz, D., Dickinson, M., Hwang, H. S., et al. 2011, A&A, 533, A119
Fischera, J., & Dopita, M. 2005, ApJ, 619, 340
Genzel, R., Tacconi, L. J., Gracia-Carpio, J., et al. 2010, MNRAS, 407, 2091
Groves, B., Dopita, M. A., Sutherland, R. S., et al. 2008, ApJS, 176, 438
Hayward, C. C., Jonsson, P., Kereš, D., et al. 2012, MNRAS, 424, 951
Hayward, C. C., Kereš, D., Jonsson, P., et al. 2011, ApJ, 743, 159
Hayward, C. C., & Smith, D. J. B. 2014, ArXiv e-prints, arXiv:1409.6332
Hayward, C. C., Lanz, L., Ashby, M. L. N., et al. 2014, ArXiv e-prints, arXiv:1402.0006
Hung, C.-L., Sanders, D. B., Casey, C. M., et al. 2013, ApJ, 778, 129
Imanishi, M., Dudley, C. C., Maiolino, R., et al. 2007, ApJS, 171, 72
Jonsson, P. 2006, MNRAS, 372, 2
Jonsson, P., Groves, B. A., & Cox, T. J. 2010, MNRAS, 403, 17
Kartaltepe, J. S., Dickinson, M., Alexander, D. M., et al. 2012, ApJ, 757, 23
Kelson, D. D. 2014, ArXiv e-prints, arXiv:1406.5191
Kennicutt, Jr., R. C. 1998, ARA&A, 36, 189
Lanz, L., Hayward, C. C., Zezas, A., et al. 2014, ApJ, 785, 39
Lanz, L., Zezas, A., Brassington, N., et al. 2013, ApJ, 768, 90
Lee, N., Sanders, D. B., Casey, C. M., et al. 2013, ApJ, 778, 131
Leitherer, C., Schaerer, D., Goldader, J. D., et al. 1999, ApJS, 123, 3
Lintott, C. J., Schawinski, K., Slosar, A., et al. 2008, MNRAS, 389, 1179
Magdis, G. E., Elbaz, D., Hwang, H. S., et al. 2010, ApJ, 720, L185
Magdis, G. E., Daddi, E., Béthermin, M., et al. 2012, ApJ, 760, 6
Magdis, G. E., Rigopoulou, D., Hopwood, R., et al. 2014, ArXiv e-prints, arXiv:1409.5605
Magnelli, B., Lutz, D., Saintonge, A., et al. 2014, A&A, 561, A86
Mentuch Cooper, E., Wilson, C. D., Foyle, K., et al. 2012, ApJ, 755, 165
Mitchell, P. D., Lacey, C. G., Cole, S., & Baugh, C. M. 2014, MNRAS, 444, 2637
Munshi, F., Christensen, C., Quinn, T. R., et al. 2014, ApJ, 781, L14
Narayanan, D., Hayward, C. C., Cox, T. J., et al. 2010a, MNRAS, 401, 1613
Narayanan, D., Dey, A., Hayward, C. C., et al. 2010b, MNRAS, 407, 1701
Noeske, K. G., Weiner, B. J., Faber, S. M., et al. 2007, ApJ, 660, L43
Oliver, S. J., Bock, J., Altieri, B., et al. 2012, MNRAS, 424, 1614
Papovich, C., Rudnick, G., Le Floc'h, E., et al. 2007, ApJ, 668, 45
Porter, L. A., Somerville, R. S., Primack, J. R., & Johansson, P. H. 2014, MNRAS, 444, 942
Rémy-Ruyer, A., Madden, S. C., Galliano, F., et al. 2014, A&A, 563, A31
Rodighiero, G., Daddi, E., Baronchelli, I., et al. 2011, ApJ, 739, L40
Saintonge, A., Kauffmann, G., Wang, J., et al. 2011, MNRAS, 415, 61
Sanders, D. B., Scoville, N. Z., & Soifer, B. T. 1991, ApJ, 370, 158
Schmidt, M. 1959, ApJ, 129, 243
Schreiber, C., Pannella, M., Elbaz, D., et al. 2014, ArXiv e-prints, arXiv:1409.5433
Snyder, G. F., Hayward, C. C., Sajina, A., et al. 2013, ApJ, 768, 168
Sparre, M., Hayward, C. C., Springel, V., et al. 2014, ArXiv e-prints, arXiv:1409.0009
Springel, V. 2005, MNRAS, 364, 1105
Springel, V., & Hernquist, L. 2003, MNRAS, 339, 289
Sturm, E., Verma, A., Graciá-Carpio, J., et al. 2010, A&A, 518, L36
Torrey, P., Vogelsberger, M., Genel, S., et al. 2014, MNRAS, 438, 1985
Veilleux, S., Kim, D.-C., & Sanders, D. B. 2002, ApJS, 143, 315
Weingartner, J. C., & Draine, B. T. 2001, ApJ, 548, 296
Whitaker, K. E., van Dokkum, P. G., Brammer, G., & Franx, M. 2012, ApJ, 754, L29
Wuyts, S., Förster Schreiber, N. M., van der Wel, A., et al. 2011, ApJ, 742, 96